Thermodynamically complete equation of state of MgO from true radiative shock temperature measurements on samples preheated to 1850 K

O. V. Fat'yanov,* P. D. Asimow,† and T. J. Ahrens‡
Division of Geological and Planetary Sciences 252-21, California Institute of Technology, Pasadena, California 91125, USA

(Received 8 August 2016; revised manuscript received 5 November 2017; published 16 January 2018)

Plate impact experiments in the 100–250 GPa pressure range were done on a ⟨100⟩ single-crystal MgO preheated before compression to 1850 K. Hot Mo(driver)-MgO targets were impacted with Mo or Ta flyers launched by the Caltech two-stage light-gas gun up to 7.5 km/s. Radiative temperatures and shock velocities were measured with 3%–4% and 1%–2% uncertainty, respectively, by a six-channel pyrometer with 3-ns time resolution, over a 500–900-nm spectral range. MgO shock front reflectivity was determined in additional experiments at 220 and 248 GPa using ≈50/50 high-temperature sapphire beam splitters. Our measurements yield accurate experimental data on the mechanical, optical, and thermodynamic properties of B1 phase MgO from 102 GPa and 3900 K to 248 GPa and 9100 K, a region not sampled by previous studies. Reported Hugoniot data for MgO initially at ambient temperature, $T = 298$ K, and the results of our current Hugoniot measurements on samples preheated to 1850 K were analyzed using the most general methods of least-squares fitting to constrain the Grüneisen model. This equation of state (EOS) was then used to construct maximum likelihood linear Hugoniots of MgO with initial temperatures from 298 to 2400 K. A parametrization of all EOS values and best-fit coefficients was done over the entire range of relevant particle velocities. Total uncertainties of all the EOS parameters and correlation coefficients for these uncertainties are also given. The predictive capabilities of our updated Mie-Grüneisen EOS were confirmed by (1) the good agreement between our Grüneisen data and five semiempirical $\gamma(V)$ models derived from porous shock data only or from combined static and shock data sets, (2) the very good agreement between our 1-bar Grüneisen values and $\gamma(T)$ at ambient pressure recalculated from reported experimental data on the adiabatic bulk modulus $K_s(T)$, and (3) the good agreement of the brightness temperatures, corrected for shock reflectivity, with the corresponding values calculated using the current EOS or predicted by other groups via first-principles molecular dynamics simulations. Our experiments showed no evidence of MgO melting up to 250 GPa and 9100 K. The highest shock temperatures exceed the extrapolated melting curve of Zerr and Boehler by >3300 K and the upper limit for the melting boundary predictions of Aguado and Madden by >2600 K and those of Strachan *et al.* by >2100 K. We show that the potential for superheating in our shock experiments is negligible and therefore out data put a lower limit on the melting curve of B1 phase MgO in P-T space close to the set of consistent independent predictions by Sun *et al.*, Liu *et al.*, and de Koker and Stixrude.

DOI: 10.1103/PhysRevB.97.024106

I. INTRODUCTION

Despite considerable theoretical and experimental effort over decades, the thermodynamic properties and melting behavior of MgO in the pressure range most interesting for geophysicists and planetary scientists, approximately 100–200 GPa, remain poorly known. The predicted melting temperature for MgO at the Earth's core-mantle boundary pressure, ≈135 GPa, ranges from 6000 to 9000 K [1–20] (Fig. 1). Direct static measurements of the melting temperature of MgO at such conditions are precluded by lack of materials that can withstand a combination of the required high pressures and temperatures. Conventional dynamic compression experiments on crystalline samples do not provide direct access to the P-T region of interest either. Upon compression along its principal Hugoniot, MgO goes from the B1 (NaCl structure) solid phase into the B2 (CsCl structure) solid phase, then into the B2-liquid coexistence region, and finally reaches the pure liquid phase above approximately 620–700 GPa [18,21]. Interpolation between the melting points measured for B1 phase at the highest attainable static pressure of ≈40 GPa [3,4] and those measured for B2 phase at approximately 470 to 650 GPa [22,23] or ≈700 GPa [21] is subject to large errors comparable to the scatter between various theoretical predictions.

None of the recently reported shock experiments to approximately 1 TPa pressure [17,18,21–24] was designed to probe even indirectly the actual melting of B1 phase MgO. These studies probed decaying [17,22,23], steady [18], or almost steady [21] states along the principal Hugoniot or quasi-isentrope [24] and so they only characterize, at best, the B2 melting curve and the B1-B2 solid-solid phase transition. Moreover, all the laser shock experiments so far published have very large uncertainties on MgO pressure and temperature due to the severe challenges associated with such measurements.

McWilliams *et al.* [22] had poor constraints on the mechanical state of their MgO samples at shock speeds below ≈17.3 km/s (i.e., pressures below ≈525 GPa) due to loss of VISAR reflectivity, high uncertainties on all pressures due to sparse calibration assuming a linear Hugoniot despite the

*fatyan1@gps.caltech.edu
†asimow@gps.caltech.edu
‡Deceased.

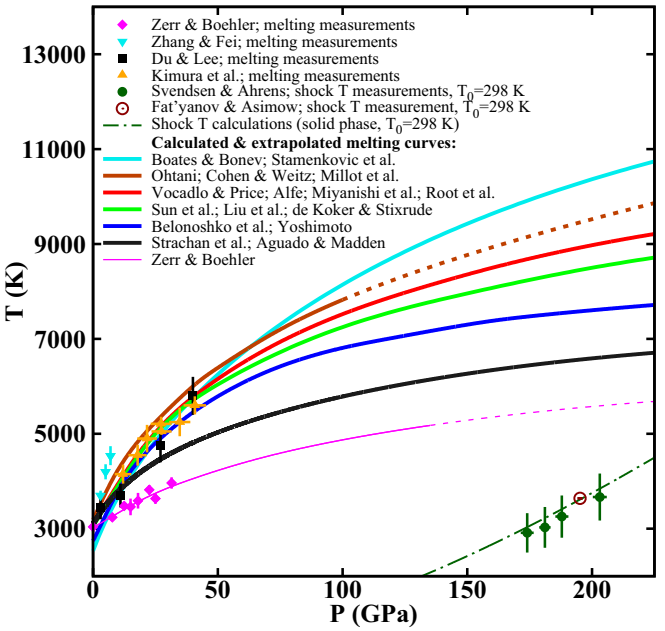

FIG. 1. Pressure-temperature diagram of MgO to 250 GPa showing the melting data [1–20] and conventional shock temperature data [25,26]. Typical uncertainties of the predicted melt lines are 100–200 K. Thicker lines indicate several melting curves that are close enough to be grouped and shown together. Dashed lines are the results of our numerical extrapolation of the reported data. All crosses are the actual error bars.

presence of phase transitions, and unknown preheating of the sample due to the lack of a radiation shield between the laser-induced plasma and the MgO target.

Bolis *et al.* [23] repeated the measurements of McWilliams *et al.* [22] with some improvements in experimental design and data analysis. First, they eliminated target preheating by employing pushers with high-Z x-ray absorbing layers optimized to minimize spurious shock wave reverberations in the studied samples. Second, they used the accurate experimental Hugoniot data of Root *et al.* [18] in addition to their own VISAR measurements at shock speeds above approximately 18.5 km/s to characterize the shock states in MgO samples. Their shock reflectivity measurements were done at two wavelengths, 532 and 1064 nm. Despite all these improvements, Bolis *et al.* [23] observed largely the same main features of MgO already reported by McWilliams *et al.* [22]. Yet, they attributed the large light intensity increase encountered during shock decay, attributed by McWilliams *et al.* to the B2 to B1 solid-solid transition, instead to a transition from melt to B2. This conclusion is in apparent disagreement with the most recent x-ray data of Smith *et al.* [21], who observed B2 melting only at approximately 700 GPa. Bolis *et al.* also completely neglected the less pronounced but still visible changes in the slopes of light emission intensity versus time (Fig. 1(b) of Ref. [23]) and temperature versus shock velocity (red lines in Fig. S9 of the Supplement to Ref. [23]) at ≈650 GPa, which are quite similar to the slightly more pronounced features at the same pressure assigned by McWilliams *et al.* to the onset of B2 phase melting [22].

The experimental data reported by Miyanishi *et al.* [17] have uncertainties too large to constrain the principal Hugoniot of MgO or the locations of its phase boundaries. The latter were determined solely by the results of their *ab initio* calculations. X-ray diffraction experiments by Coppari *et al.* [24] were done for ramp-compression loading only, which generates significantly lower temperature compared to that along the principal Hugoniot at the same pressure. These experiments obtained unique information on directly-probed crystalline phases at these conditions, but they were not designed to measure temperature.

Root *et al.* [18] performed high-accuracy mechanical measurements along the principal Hugoniot of MgO and used that data as constraints for advanced quantum calculations that predicted locations of the phase boundaries and melting curves. However, no shock temperature was measured in their experiments, which leaves their conclusions about MgO thermodynamics and B1 phase high-pressure melting at the stage of reasonable but still untested hypotheses.

Smith *et al.* [21] demonstrated the most comprehensive approach so far. They performed simultaneous measurements of all important MgO parameters using x-ray diffraction, velocity interferometry, and shock pyrometry. Unfortunately, the complexity of their measurements led to experimental uncertainties too large for accurate interpolation between their high-pressure B2 phase data and available low-pressure B1 phase data. Laser-driven shock wave loading in their experiments was not completely steady. As in all other laser-driven pyrometry experiments to date, their temperature measurements were calibrated to shock-compressed quartz, which is not a primary standard and has been shown to give poor accuracy [26]. The range of their reported B1-B2 and B2-melt transition pressures was more than 50 GPa and the lowest shock temperature uncertainty was ≈1000 K.

Thus a review of all the studies to date in the scientific literature shows that further exploration of the phase diagram of MgO is needed to support understanding of lower-mantle phase equilibria and other studies. In theory, the desired combination of P-T parameters could be easily generated in shock-compressed porous samples. However, this approach was found impractical mainly because the measurements on shock compressed porous samples with modern diagnostic tools have not yet demonstrated enough accuracy in shock velocity, sound speed, or temperature to resolve MgO melting. To study mechanical, thermal, and optical properties of MgO above approximately 100 GPa and 5000 K and to get a better constraint on the location of its high-pressure melting curve, we developed a technique for radiative shock temperature measurements on MgO crystals preheated up to 2300 K [27]. In this report, we summarize the results from 12 experiments done at initial temperature of 1850 K, in a configuration for simultaneous measurements of shock temperature and shock velocity from time-resolved radiance histories. Preliminary results from the first six, largely exploratory, experiments of this series were reported in Ref. [28]. In later experiments and additional tests we were able to identify at least five major phenomena unaccounted for or even unexpected in our earlier studies. Related systematic errors and the required correction factors are discussed in Sec. II along with the description of our experimental technique.

To construct the EOS for solid MgO, we reanalyzed its principal Hugoniot first, taking into account the most recent accurate data reported by other groups [29]. This new D versus U line and the updated hot Mo Hugoniot [30] were then used for the analysis of the hot MgO Hugoniot and its Grüneisen function. These results are summarized in Sec. III.

Next, the results of radiative temperature and shock front reflectivity measurements in MgO preheated to 1850 K were analyzed using the most recent information on the required correction factors. Our final true shock temperatures closely match the results of our most accurate EOS model prediction for the solid B1 phase of MgO over the entire range of shock pressures studied. This analysis is summarized in Sec. IV.

Finally, we estimated the maximum degree of superheating in our experiments and its potential impact on our results and conclusions about the MgO melting curve. Our analysis took into account the most reliable experimental data and the most recent results of proper molecular dynamics simulations found in the literature. These results and the constraints on the location of B1 phase MgO melting curve at approximately 200–250 GPa by our data are discussed in Sec. V.

II. EXPERIMENTAL APPROACH

The experimental technique applied in this work combined two previously developed methods: high-speed, plate impact shock experiments on samples preheated up to 1932 K [31] and conventional fast multiwavelength optical pyrometry [32]. The main features of the experimental design were already reported in sufficient detail [28]. Salient features of the particular experiments reported in this work can be also found in Sec. I A of Ref. [33]. A comprehensive review of the Caltech six-channel pyrometer operation and calibration can be found elsewhere [26]. Therefore we give only a brief description of the most essential issues, shock target parameters, and newly developed procedures for the data acquisition and analysis.

Most experiments were done using the "unwindowed" target configuration with a 3-mm-thick MgO crystal [Fig. 2(a)]. For shock front reflectivity measurements (shots 406 and 411 only) we employed the "windowed" configuration [Fig. 2(b)] with an ≈1.5-mm-thick MgO crystal backed by an ≈1.5-mm-thick stack of 5 sapphire windows (12.7-mm diameter by 0.25-mm-thick each) separated by five annular Mo shims made of 25-μm-thick foil.

The phenomena unaccounted for in our earlier studies include (1) initial MgO temperatures approximately 65–70 K lower than those we reported in Ref. [28] (see Sec. I B of Ref. [33] for the details of thermal gradient measurements), (2) an average 6.4% reduction of the pyrometer mirror reflectivity (or absolute intensity correction factor of 0.936) after it was exposed for a few seconds to heat from the hot target (Sec. I C of Ref. [33]), (3) an average $22 \pm 4\%$ reflectivity of the MgO shock front measured at 220 and 248 GPa shock pressure (see Sec. IV B), (4) up to ≈21% lower electronic output response of the pyrometer photodetectors to short, approximately 10^{-8} to 10^{-7} s, optical pulses from shock experiments compared to long, approximately 10^{-3} s, calibration pulses [26], and (5) formation of an 18 ± 2-μm-thick (as measured at room T) black layer of Ti-doped MgO at the impact side that reduced the shock travel distance "seen" by the shock pyrometer in all experiments with Ti foil (shots 389–411). After correcting the systematic errors induced by these effects, we report herein fairly good agreement between the results of our model prediction and experimental values.

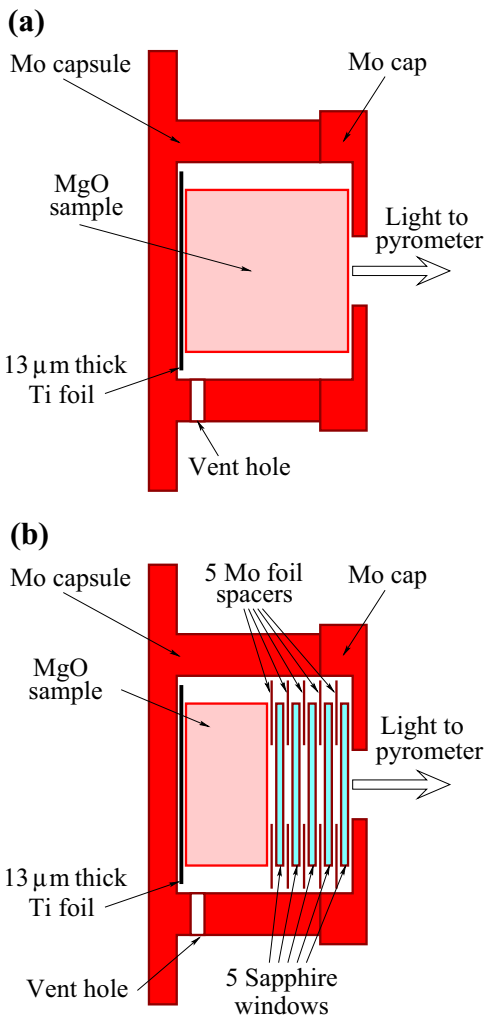

FIG. 2. Schematics of hot MgO targets (not to scale; horizontal dimensions are stretched relative to vertical in order to show the details of high-T sapphire beam splitter): (a) "unwindowed" configuration for conventional shock temperature measurements (used in shots 389–405 and 407–410 and with no Ti foil in shots 383–387) and (b) "windowed" configuration for shock front reflectivity measurements (shots 406 and 411 only).

III. HUGONIOTS AND GRÜNEISEN MODEL

Analysis of MgO Hugoniots at 298, 1850, and 2300 K was done in a manner similar to that applied for Mo [30] except that we have data at 1850 K (as well as another 17 experiments at 2300 K to be analyzed and reported in a forthcoming paper) but no data at 1673 K.

A. Room T data

For the analysis of the principal Hugoniot of MgO, we selected D versus U data from the following sources: Refs. [29], [44] (p. 312), [45], and [46]. All low-stress data points that show two-wave structure [29,47], with $U < 2$ km/s or

TABLE I. Comparison of the maximum likelihood principal Hugoniots for MgO obtained from the D vs U and U vs D fits. Insignificant digits are shown to emphasize the differences. The opposite sign of absolute slope and intercept differences confirms strong anticorrelation of the best linear fit parameters. The reduced misfit was calculated for $n = 20$ data points and $q = 2$ parameters or $(n - q) = 18$ degrees of freedom.

Parameter	D versus U fit	U versus D fit	Absolute difference
Intercept, a	6.64199	6.63649	−0.00550
Intercept uncertainty, σ_a	0.0467817	0.0468205	3.88×10^{-5}
Slope, b	1.35286	1.35450	0.00164
Slope uncertainty, σ_b	0.013779	0.013790	1.12×10^{-5}
Uncertainty correlation, $cor(\sigma_a,\sigma_b)$	−0.966487	−0.966520	-3.3×10^{-5}
Absolute reduced misfit, $\chi_0^2/(n-q)$	0.182478	0.182551	7.3×10^{-5}

$D < 9.8$ km/s, were excluded. All high pressure data points above $U = 5$ km/s, including the accurate data of Root *et al.* [18], were excluded because of noticeable nonlinearity on the Hugoniot extended into this range [18] compared to the range relevant to this study. Data of Miyanishi *et al.* [17] were excluded from our analysis because of high uncertainties and scatter. We also excluded the "absolute" EOS data set of Fratanduono *et al.* [29] (upper part of their Table II) and used only their high accuracy impedance match data set (lower part of their Table II). These data were not obtained by using any *a priori* assumed MgO Hugoniot. Instead, the authors computed the MgO shock velocity in these experiments from the known Hugoniots of their Al or Ta impactors [48] via an impedance match solution to the conservation equations from impact and MgO particle velocities accurately measured by photonic Doppler velocimetry (PDV) [29].

The general least-squares fitting procedure [49,50] used earlier for Mo [30] was applied to the MgO data analysis (Table I). Our best fit linear Hugoniot for the room-T MgO, valid for the U range from 2.2 to 4.8 km/s, is $D = 6.64(\pm0.05) + 1.353(\pm0.014)\,U$, with correlation coefficient of $-0.97(\pm0.01)$ between the uncertainties for slope and intercept. The uncertainty in shock velocity for any fixed value of particle velocity from this range does not exceed ±0.02 km/s at the 1σ level.

B. 1850-K Hugoniot

Shock parameters from 12 experiments on MgO with initial temperature of 1850 ± 10 K are summarized in Tables II and III.

Table IV summarizes the results of applying three Grüneisen models to the 1850-K data analysis. As in the case of 1673-K Mo [30], χ_1^2 represents the misfit between the experimental data and the most likely corresponding points along the nonlinear high-T Hugoniot obtained by a Mie-Grüneisen offset from the principal Hugoniot; χ_2^2 represents the misfit between those points along the nonlinear high-T model Hugoniot and corresponding most likely points along a linear high-T Hugoniot; and finally, χ^2 represents the misfit between the original high-T Hugoniot data and the most likely points along the linear model high-T Hugoniots. No intermediate maximum likelihood values were obtained for the conventional unconstrained and double-constrained fits (see below) shown in lines 1 and 5 of Table IV, respectively.

The difference of specific internal energies of MgO at room T and 1850 K was calculated from the reported specific heat at constant pressure data [57–60]. The density of MgO at 1850 K was calculated from available thermal expansion data [59–62]. The uncertainties of density and specific internal energy difference for MgO were evaluated as root-mean square deviations from the average values of four sources, assuming uncorrelated data. Full uncertainties took into account

TABLE II. Summary of our experimental Hugoniot data for 1850 K MgO. Numbers in parentheses are 1σ uncertainties for the last significant digit(s).

Shot number	Flyer	U_f (km/s)	Measured D (km/s)	Model deviation, $(D^\star - D)/\sigma_D$	Measured U (km/s)	Model deviation, $(U^\star - U)/\sigma_U$
390	Mo	4.401(8)	10.24(7)	−0.24	2.976(10)	0.05
387	Mo	4.563(6)	10.3(3)	0.25	3.09(3)	−0.03
389	Mo	5.093(4)	10.78(6)	0.85	3.433(10)	−0.18
384	Mo	6.081(5)	11.62(15)	0.49	4.077(15)	−0.07
383	Mo	6.540(7)	11.8(2)	1.54	4.39(2)	−0.21
391	Ta	6.589(11)	12.60(5)	1.35	4.810(14)	−0.45
405	Ta	6.943(13)	13.09(5)	−1.64	5.049(16)	0.60
406	Ta	6.951(2)	13.0(2)	0.12	5.07(2)	−0.02
407	Ta	7.268(10)	13.38(6)	−1.04	5.285(15)	0.32
408	Ta	7.344(2)	13.3(2)	0.55	5.36(2)	−0.07
410	Ta	7.512(1)	13.51(10)	0.49	5.472(16)	−0.10
411	Ta	7.507(11)	13.6(2)	−0.26	5.46(3)	0.05

TABLE III. Summary of our experimental initial and final shock parameters for 1850-K MgO. Numbers in parentheses are 1σ uncertainties for the last significant digit(s).

	Initial parameters		Shock density		Shock pressure	
Shot number	Temperature T_0 (K)	Density ρ_0 (g/cm^3)	Measured ρ (g/cm^3)	Model deviation, $(\rho^\star-\rho)/\sigma_\rho$	Measured P (GPa)	Model deviation, $(P^\star-P)/\sigma_P$
390	1847(10)	3.345(2)	4.72(2)	0.13	102(1)	−0.08
387	1857(10)	3.343(2)	4.78(8)	−0.23	106(2)	0.27
389	1847(10)	3.345(2)	4.91(2)	−0.72	124(1)	0.44
384	1857(10)	3.343(2)	5.15(5)	−0.44	158(2)	0.36
383	1838(10)	3.346(2)	5.33(7)	−1.35	173(3)	1.03
391	1845(10)	3.345(2)	5.41(2)	−1.25	203(1)	0.87
405	1846(10)	3.345(2)	5.45(2)	1.24	221(1)	−0.91
406	1846(10)	3.345(2)	5.48(7)	−0.12	220(3)	0.10
407	1846(10)	3.345(2)	5.53(3)	0.59	236(1)	−0.65
408	1847(10)	3.345(2)	5.60(8)	−0.46	238(3)	0.45
410	1845(10)	3.345(2)	5.62(4)	−0.48	247(2)	0.36
411	1846(10)	3.345(2)	5.59(7)	0.20	248(3)	−0.18

variations of thermodynamic parameters with initial temperature, known in these experiments to ±10 K (Table III).

An unconstrained linear fit of hot MgO D versus U data gives a hot Hugoniot slope higher than that of our best fit room-T Hugoniot (first row of Table IV). As was discussed for Mo in Ref. [63], this would eventually lead to higher shock velocity on the high-temperature Hugoniot than that on the room-T Hugoniot at equal particle velocity and, therefore, negative values of the thermal expansion coefficient at high pressure.

Although an EOS with negative Grüneisen functions (and related negative thermal expansion coefficients) allowed the authors of Ref. [64] to explain and describe the anomalies observed in shock-compressed porous silicates, this approach is not applicable to MgO for two reasons. First, an alternative model that uses only positive Grüneisen coefficients can also reproduce the same unusual behavior of some phase-changing porous substances quite well [65]. Second, the rare anomaly of higher density in shock-compressed porous samples than in fully dense solid samples at equal pressure [64,65] has never been observed in metals [64] or MgO [66].

Therefore a hot Hugoniot fit with slope higher than that of the corresponding room-T Hugoniot should not be extrapolated beyond the calibrated range. Furthermore, the range in offsets between the unconstrained hot linear Hugoniot and the cold linear Hugoniot yields an unacceptably large range of apparent γ_0 values (first row of Table IV). These results and subsequent data analysis indicate that the higher slope of the unconstrained hot MgO Hugoniot is merely an artifact caused by data uncertainties and scatter. Unlike our hot Mo experiments [63,67,68], primarily designed to yield accurate shock velocity data, these hot MgO experiments were mainly aimed at radiative temperature measurements. Shock transit times in MgO samples are additional information that we were able to extract from time-resolved radiance histories.

Instead, we first attempted three single-constrained fits using the three most popular models for the volume dependence of the Grüneisen parameter; all three results are similar in goodness of fit. However, as in the case of hot Mo [30], both Al'tshuler's [54] and Molodets' model forms [55,56] give γ_0 values that are significantly lower than 1.54 ± 0.02, the value computed from the known thermodynamic parameters of MgO [57–62,69–71]. Nearly a dozen other reported Grüneisen models with up to four fitting parameters [34–40] that we tried later did not improve the quality of fit (see Sec. II B of Ref. [33]). Therefore, with due regard to its limited applicability over wide density ranges and incorrect asymptotic value at infinite pressure, we selected again the Los Alamos laboratory's simple $\gamma = \gamma_0\, V/V_0$ model [51–53] for the description of MgO shock parameters over the particular narrow range of our study.

TABLE IV. Comparison of 1850-K MgO Hugoniot fits for different Grüneisen models.

Constraint	γ_0	χ_1^2	D to U linear fit	χ_2^2	χ^2
–	1.344 to 1.496	–	6.12(12) + 1.36(3) U	–	0.82
$\gamma = \gamma_0\, V/V_0$ [a]	1.362	0.95	6.1958(15) + 1.3411(3) U	1.2×10^{-4}	1.04
$\gamma = \frac{2}{3} + (\gamma_0 - \frac{2}{3})\,(V/V_0)^{\frac{\gamma_0}{\gamma_0-2/3}}$ [b]	1.283	0.86	6.142(2) + 1.3553(5) U	2.6×10^{-4}	0.94
$\gamma = \frac{2}{3} + \frac{2V}{[1+2/(\gamma_0-2/3)]V_0-V}$ [c]	1.122	0.86	6.099(4) + 1.3664(8) U	7.6×10^{-4}	0.92
$\gamma = \gamma_0\, V/V_0$ and $D = c + s\,U$	1.432 to 1.436	–	6.24115 + 1.33774 U	–	0.89

[a]References [51–53].
[b]Reference [54].
[c]References [55,56].

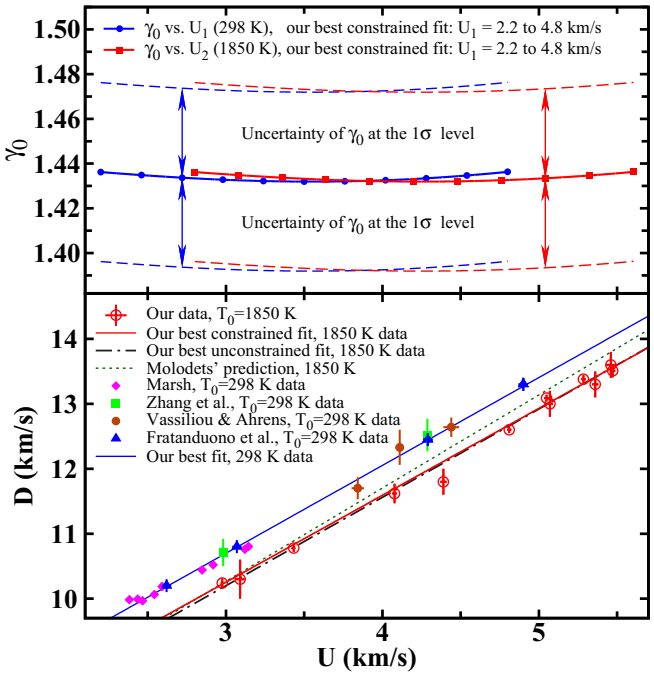

FIG. 3. Maximum likelihood fits to the reported 298-K [29,44–46] and our 1850-K D vs U data for MgO (bottom) and analytically computed values of γ_0 from the double-constrained fit to hot Hugoniot (top). The D-U fit from the last line of Table IV was used to compute γ_0 for U_1 from 2.2 to 4.8 km/s. Note the particle velocity (horizontal) offset between the matching $\gamma_0(U_1)$ and $\gamma_0(U_2)$ curves and its monotonic increase with U. All crosses indicate the actual error bars. Although the 1850-K Hugoniot of Molodets [56] shown here evidently diverges from the data, his 300-K Hugoniot (not shown) nearly coincides with our best fit line to 298-K data.

Applying the most advanced least-squares methods [30,49,50] finally allowed us to extract a quite accurate maximum likelihood Grüneisen model and Hugoniot for MgO preheated to 1850 K before shock compression that lacks the slope problem of the unconstrained linear fit. This double-constrained fit, our preferred result, is shown in the last row of Table IV.

All the 298- and 1850-K D-U data and the corresponding 298-K and 1850-K linear Hugoniots are plotted in Fig. 3 along with the resulting best-constrained maximum likelihood Grüneisen function and its error bounds. Note that we use the notation U_1 to refer to the particle velocity of a point on the 298-K principal Hugoniot and the notation U_2 to refer to the particle velocity of a corresponding point at the same volume along a preheated Hugoniot. We find that our best-fit value of $\gamma_0 = 1.43 \pm 0.04$, though lower than that calculated from reported ambient experimental K_s data [69–71], is consistent with numerous literature values of γ_0 obtained from semiempirical EOS: 1.49 ± 0.03 [72], 1.46 ± 0.02 and 1.47 ± 0.02 [73], 1.442 ± 0.015 and 1.431 ± 0.014 [74], and 1.41 to 1.42 [75].

C. Synthetic hot Hugoniots

The best synthetic Hugoniots for MgO at 1850 and 2300 K initial temperatures accounting for correlated uncertainties for all the required parameters (γ_0, slope and intercept of room-T Hugoniot, densities of ambient and hot MgO, and internal energy difference between the ambient and hot MgO) [33] were determined by a sequence of fitting and Monte Carlo procedures similar to those applied earlier for the case of hot Mo [30]. The resulting fits are presented in Table V. Polynomial coefficients for the parameters of a linear MgO Hugoniot from any initial temperature in the range 298 to 2400 K are summarized in Table VI.

D. Validation of our Grüneisen model

1. *Comparison with reported empirical and analytical Grüneisen functions based on porous shock compression*

To validate our choice of Grüneisen model, we first made a direct comparison with the most accurate experimental values obtained and reported for MgO by other shock compression groups [76–78] (Fig. 4). Bushman and Lomonosov tabulated values of the volume- and internal energy-dependent $\gamma(V,E)$ from their caloric KEOS5 model [78] only along several initially porous MgO Hugoniots. Our preheated 1850-K Hugoniot roughly matches, in both (U,D) and (V,E) space, their data for 6% initial porosity ($\rho_{00} = \rho_0/1.06$). The solid black line shown in Fig. 4 is the average of $\gamma(V,E)$ curves for their full density and $m = 1.06$ porous Hugoniots at equal shock-compressed volume.

Although the Grüneisen functions constructed by various groups are based largely on the same porous MgO experimental data [44,76], there is poor mutual agreement among them or with our model (based on preheated MgO data), when examined at low compression, i.e., $V/V_0 \geqslant 0.8$. However, there is much better agreement for the whole range of compressions considered here, $0.76 \geqslant V/V_0 \geqslant 0.64$, between three γ models: the best-fit function $\gamma(V) = 0.5 + 1.04(V/V_0)^{1.93}$ of Al'tshuler and Sharipdzhanov [77], the tabular $\gamma(V,E)$ data of Bushman and Lomonosov [78], and our model of $\gamma(V) = 1.43(4)V/V_0$. All three models clearly converge at higher pressure (or $0.7 \geqslant V/V_0 \geqslant 0.6$), within the $\pm 3\%$ level of their estimated relative uncertainties. We emphasize that we have not used any porous MgO data in our analysis and the authors of Refs. [76–78] did not use any preheated MgO

TABLE V. Hugoniots for MgO from various initial temperature. The first two lines are fits to the experimental data. The last two lines are predictions of our EOS model. Numbers in parentheses are 1σ uncertainties for the last significant digit(s).

T_0 (K)	ρ_0 (g/cm^3)	ΔE_0 (J/g)	$a(\sigma_a)$ (km/s)	$b(\sigma_b)$	$cor(\sigma_a,\sigma_b)$
298(5)	3.584(2)	–	6.64(5)	1.353(14)	−0.97(1)
1850(10)	3.344(3)	1942(14)	6.24(12)	1.34(3)	−0.98(2)
1850	3.344(2)	1942(6)	6.24(5)	1.337(9)	−0.98(2)
2300	3.260(2)	2570(8)	6.12(5)	1.332(10)	−0.98(2)

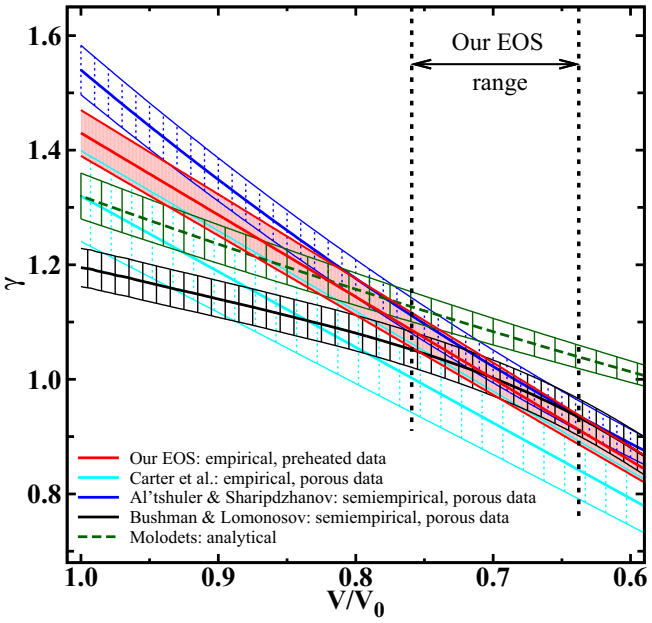

FIG. 4. Comparison of our $\gamma(V)$ model with other reported empirical [76], semiempirical [77,78], and analytical models [56] for shock-compressed MgO. The shaded areas indicate uncertainties estimated by us.

data. Good agreement between our $\gamma(V)$ fit and two different advanced semiempirical Grüneisen functions [77,78], over the volume range constrained by our EOS, demonstrates the accuracy of our statistical analysis.

As seen in Fig. 4, the function $\gamma(V) = 1.32V/V_0$, reported by Carter *et al.* shows only marginal agreement with other semiempirical or empirical models. We estimated ±6% uncertainty from the scatter of their $(\partial E/\partial P)_V$ data (Ref. [76], Fig. 18). On the other hand, the analytical model of Molodets [56] gives values similar to the fit of Al'tshuler and Sharipdzhanov [77] over a limited volume range. With uncertainties estimated via a standard error propagation analysis for γ_0 only, assuming all other model parameters (V and V_0) to be exact, the model of Molodets may be valid at low compression, $V/V_0 \geqslant 0.71$. At higher pressure, $V/V_0 \leqslant 0.71$, it apparently fails to predict any experimental Grüneisen data for shocked MgO.

2. *Comparison with reported semiempirical Grüneisen functions from static or joint static-shock data*

Another possible validation of our Grüneisen model is direct comparison with the values inferred from the analysis of static compression or joint fitting to static and shock compression data. Plots of 14 popular $\gamma(V)$ functions [41–43,72–75,80,84,85] along with our data for MgO can be seen in Sec. III of Ref. [33]. The systematic differences between the various reported semiempirical Grüneisen models of this type are quite large. Nevertheless, we find three curves in agreement with our $\gamma(V)$ function within the quoted or estimated uncertainties. These include the model of Dorogokupets and Dewaele [80] [$\gamma(V) = 0.75 + 0.75\,(V/V_0)^{2.96}$] and two models given by Kennett and Jackson [73], one based on nonlinear inversion of 14 data sets [$\gamma(V) = 1.46(2)\,(V/V_0)^{1.14(5)}$] and one restricted to inversion of 9 data sets that do not depend on empirical pressure scales [$\gamma(V) = 1.47(2)\,(V/V_0)^{0.98(5)}$]. More discussion on $\gamma(V)$ functions from primarily static compression data can be found in Sec. III of Ref. [33].

3. *Prediction of macroscopic $\gamma(T)$ at 1 bar*

To further validate our choice of Grüneisen model, we compared the macroscopic Grüneisen coefficients at 1 bar computed (1) directly from our $\gamma(V)$ model,

$$\gamma_1(T) = \gamma_0\, V(T)/V_0 = \gamma_0 \exp\left(\int_{T_0}^{T} \alpha(T)\, dT\right), \quad (1)$$

and (2) from the family of bulk sound speed values,

$$\gamma_2(T) = \alpha(T)\, V(T)\, K_s(T)/C_p(T) = \alpha(T)\, c_0(T)^2/C_p(T), \quad (2)$$

TABLE VI. Summary of the best fit parameters of the MgO Hugoniot predicted by our EOS as a function of the initial temperature, $D = a(T) + b(T)\,U$. All parameters are expressed as $Q(T) = k_0 + k_1\,(T-298) + k_2\,(T-298)^2 + k_3\,(T-298)^3$, where T is the absolute temperature in K.[a] Every individual Hugoniot is valid for its own range of particle velocities from $U^{\min}(T)$ to $U^{\max}(T)$. This range varies with the initial MgO temperature from 2.2–4.8 km/s at 298 K to 3.1–6.0 km/s at 2400 K.

Parameter	Best fit coefficients			
	$k0$	$k1$	$k2$	$k3$
Initial density, $\rho_0(T)$ (g/cm^3)	3.584	-1.258×10^{-4}	-2.108×10^{-8}	1.580×10^{-12}
Density uncertainty, $\sigma_{\rho_0}(T)$ (g/cm^3)	0.002	–	–	–
Intercept, $a(T)$ (km/s)	6.64	-2.314×10^{-4}	-1.551×10^{-8}	–
Intercept uncertainty, $\sigma_a(T)$ (km/s)	0.05 ($T < 2340$ K) 0.06 ($T \geqslant 2340$ K)	–	–	–
Slope, $b(T)$	1.353	-8.015×10^{-6}	-1.292×10^{-9}	–
Slope uncertainty, $\sigma_b(T)$	0.014	–	–	–
Correlation of uncertainties, $cor(\sigma_a,\sigma_b)$	−0.98(2)	–	–	–
Lower limit, $U^{\min}(T)$ (km/s)	2.2	2.970×10^{-4}	5.825×10^{-8}	–
Upper limit, $U^{\max}(T)$ (km/s)	4.8	3.865×10^{-4}	8.516×10^{-8}	–

[a]For example, the initial density of MgO from 298 to 2400 K is $\rho_0(T) = [3.584 - 1.258\times10^{-4}\,(T-298) - 2.108\times10^{-8}\,(T-298)^2 + 1.580\times10^{-12}\,(T-298)^3]$ g/cm^3.

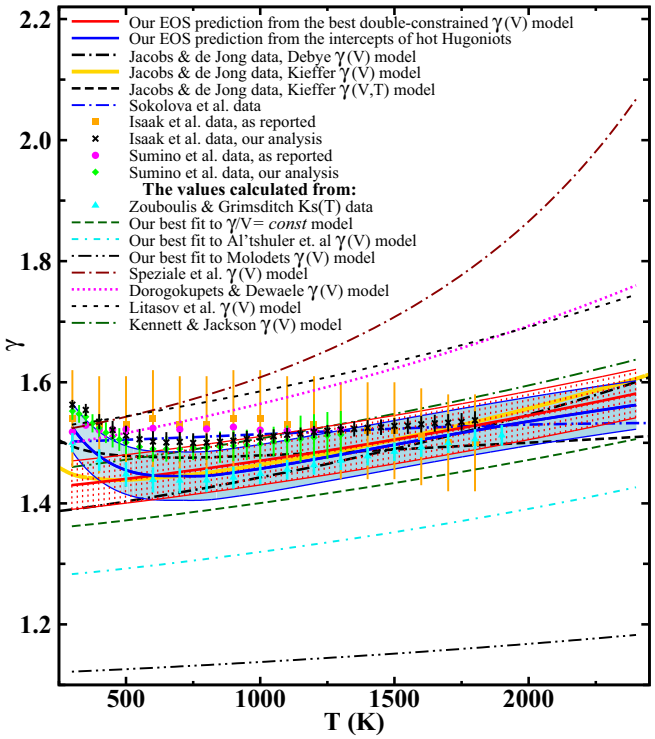

FIG. 5. Comparison of our macroscopic Grüneisen parameters at 1 bar with the reported experimental $\gamma(T)$ values [70,71], results of our calculations from the reported measurements of $K_s(T)$ [69–71], and the values predicted by other reported EOS [60,72–74,79,80,84,85]. Two shaded areas indicate the uncertainties of our data. Some curves are not plotted because they overlie our model fits precisely and the curves would obscure one another: $\gamma(T)$ computed from the third-order Birch-Murnaghan EOS of Tange *et al.* [74] matches the solid red line below 1000 K; that obtained from the Vinet EOS of Tange *et al.* [74] matches the solid red line above 1000 K; and Kennett and Jackson's second model [73] coincides with the upper thin solid red line representing $\gamma_1(T) + \sigma_{\gamma_1}$.

where $\gamma_0 = 1.43 \pm 0.04$ is our model value, $\alpha(T)$ is the volume thermal expansion coefficient, $K_s(T)$ is the isentropic compression bulk modulus, $c_0(T)$ is the bulk sound speed, and $C_p(T)$ is specific heat (all parameters at 1 bar). A single-crystal MgO shocked along ⟨100⟩ orientation (1) has negligible shear strength above 11.2 GPa [81,82] and (2) does not undergo phase transitions to ≈226 GPa on the room-T Hugoniot [29] and to ≈248 GPa on 1850-K Hugoniot (Sec. IV). These properties of MgO are also confirmed by good agreement between the intercept of room-T Hugoniot, 6.64 ± 0.05 km/s, and the values of bulk sound speed at ambient conditions, 6.63 to 6.76 km/s, recalculated from the reported adiabatic bulk modulus data (157.3 to 163.9 GPa) [69–71,83]. Therefore, as in the case of Mo [30], $c_0(T)$ is approximately equal to $a(T)$, the hot Hugoniot intercept. Equation (2) then becomes

$$\gamma_2(T) = \alpha(T)\, a(T)^2 / C_p(T). \tag{3}$$

The results, shown in Fig. 5, indicate very good agreement between the model Grüneisen values computed by these two approaches at any temperature above 500 K. We emphasize that our primary Grüneisen model was constructed as an offset from the room-T Hugoniot with (P,T) states ranging from approximately (76 GPa, 950 K) at $U_1 = 2.2$ km/s to approximately (226 GPa, 4500 K) at $U_1 = 4.8$ km/s, i.e., for temperatures well above ≈1000 K. Therefore our mainly empirical EOS gives self-consistent predictions for the asymptotic low-pressure values of γ versus T over the entire temperature range where the EOS (constructed for solid B1 phase only) remains valid. Large apparent disagreements between the reported experimental $\gamma(T)$ values and those that result when our data are fits to the functional forms of the Al'tshuler *et al.* and Molodets models confirm the validity of our choice of the simplest form for volume dependence, $\gamma = \gamma_0\, V/V_0$.

Figure 5 further demonstrates that both our Grüneisen functions show excellent agreement with the $\gamma(T)$ values recalculated from the experimental $K_s(T)$ data of Zouboulis and Grimsditch [69] from ≈500 K. The maximum relative difference between $\gamma(T)$ calculated from their values and our $\gamma_2(T)$, calculated from the hot Hugoniot intercepts via Eq. (3), does not exceed 1% over the entire range of their measurements, from room T to 1900 K. Comparison of our Grüneisen values with those reported by Sumino *et al.* [70] and Isaak *et al.* [71] shows reasonable agreement within the quoted uncertainties. The authors of Refs. [70] and [71] each based their analysis of $\gamma(T)$ on the best MgO thermal expansion data available at that time, with ±5% relative uncertainty, and extrapolated above 1250 K (see Ref. [71], footnote "a" to Table IV, for example). Therefore we reanalyzed their Grüneisen values and uncertainties using their primary experimental $K_s(T)$ values [70,71] and the most recent experimental data on thermal expansion [59–62] and C_p [57–60], the same values used in our EOS. The updated values of $\gamma(T)$, with uncertainties about five times smaller than those originally reported (Supplemental Material data files [33]), are still in reasonable agreement with our data from approximately 1000 to 1500 K and are in good agreement from 1500 to 1800 K. It should be noted that the authors of Ref. [71] explicitly acknowledged that their room-temperature K_s value is 0.9% higher than that reported by other groups. However, comparison with either set of reported 1-bar high-temperature *static* experiments clearly confirms the very good predictive capabilities of our EOS constructed primarily from the *shock* data.

Our $\gamma(T)$ data above ≈500 K agree well with the predictions of the EOS of Jacobs and de Jong with either Kieffer or Debye quasiharmonic specific heat models [79]. The same level of agreement is seen between our data and $\gamma(T)$ values recalculated from either $\gamma(V)$ functions of Kennett and Jackson [73] up to 1200 K, whereas we find agreement within error with the tabular values of Sokolova *et al.* [84] above 1200 K. Even better agreement is observed with the data of Tange *et al.* for the Vinet model [74]. Their values are ⩽0.5% higher than our $\gamma_1(T)$ data below 1000 K and completely indistinguishable at all higher temperatures.

As Fig. 5 shows, only a subset of MgO equations of state constructed primarily from *static* compression data [73,74,79,84] correctly predict $\gamma(T)$ at 1 bar. Other popular EOS formulations reported in the literature [72,80,85] clearly lack this capability. Analysis of experimental compression data

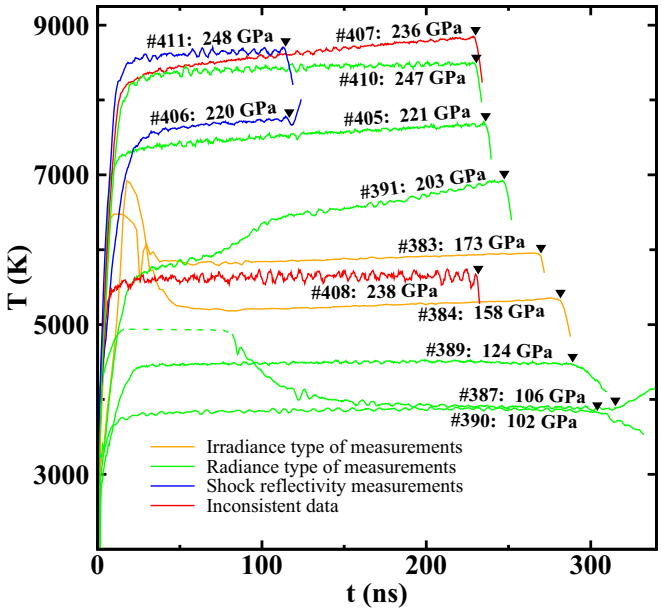

FIG. 6. Brightness temperature profiles (analyzed assuming $r = 0.02$) from all our experiments. Records are labeled with the corresponding shot numbers; see Sec. I A of Ref. [33] for description of salient features of each shot. Triangles indicate arrival times of shock waves at the free surfaces of MgO samples.

with the most recent accurate thermal expansion values shows that the role of anharmonicity in the high-temperature behavior of MgO [79,80] may have been somewhat exaggerated.

IV. SHOCK TEMPERATURES OF MGO PREHEATED TO 1850 K

A total of 12 experiments were performed to measure shock temperatures in MgO preheated before compression. Ten of them were done in a conventional geometry while two experiments were specially designed to measure the shock front reflectivity, employing thinner MgO samples (approximately 1.5 mm instead of 3 mm) backed by a stack of five thin sapphire windows (Fig. 2). The multiple parallel layers of sapphire formed a partially transparent mirror that reflected at 1850-K 46% to 47% of light emitted by the MgO towards the shock pyrometer back to the sample free surface and radiative shock front.

A. Shock temperature analysis

Brightness temperature profiles from all 12 shots are shown in Fig. 6. The values listed in Table VII for each experiment were extracted at the end of the useful portion of each spectral radiance record, just prior to shock wave arrival at the MgO free surface. This approach, conventional in shock pyrometry, was selected for several reasons. First, it takes the values of spectral radiance corresponding to the maximum thickness of the shock-compressed layer. That, in turn, maximizes the optical thickness of the emitting layer and makes its radiative properties approach more closely those of a black or a grey body. Second, it eliminates any potential radiometric errors due to light absorption in the layer of unshocked material between the propagating shock front and the stationary free surface. Third, the initial temperature of MgO was monitored at the back surface of the capsule and, therefore, was most accurately known there. Fourth, our detailed calibration studies [26] revealed that the difference between the static and dynamic response of our amplified photodetectors decreased as the input light pulse duration increased. Therefore the errors in the corresponding correction factors are minimized at the end of useful radiance records.

For experiments 389 and 390, which exhibited a 60-K shock T decrease over the last 70 ns of shock travel (as discussed in Sec. I A of Ref. [33]), not seen in any other experiments, we extrapolated the steady portion of their radiative temperature histories (approximately 30 to 220 ns) to the time of shock arrival at the MgO free surface instead of taking the actual shock T values from the records. The validity of this approach was confirmed by several observations. First, the decrease in radiance was not seen in any other experiment, not even in shot 387, done at nearly the same shock conditions as 390. Second, there are no phase transitions or any other known transformations in MgO in the range of pressures and temperatures that could introduce any time-dependent response to shock loading. Third, this approach resulted in a much better agreement between the measurements and the predictions of our EOS. Therefore the observed anomalies in behavior, though observed twice, were most probably experimental artifacts caused by the complexity of conflicting engineering requirements for the hot target design and assembly rather than some intrinsic phenomenon in MgO.

The time-dependent temperature profiles in all experiments with Ti foil (389–411) show that an optically thick radiative layer was established within 20–30 ns over the whole range of studied pressures. Gradual increases in pyrometer signals after the initial transient were caused by the transient response of amplified photodetectors and by multiple reflections of radiation from the free surface of MgO back to the shock front. There were no significant positive longitudinal thermal gradients in the targets and no detectable optical absorption in hot MgO at any wavelength longer than approximately 550 nm. Normalized radiance histories from most experiments with Ti foil looked very similar to that observed in NaCl shock compressed at room T (see Fig. 8 of Ref. [26]).

Analysis of the shock temperature data was done in several steps. First, we computed and compared quasibrightness temperatures for all pyrometer channels. The agreement between these values is a necessary condition for thermal equilibrium in the shock-compressed state. Then, we performed unweighted and weighted nonlinear fits for the temperature only using a constant emissivity of 0.91 for all pyrometer wavelengths. This value was obtained from the estimated 7.6% Fresnel reflection at the MgO-vacuum interface and 2% reflectivity of the shock front. These temperatures were found by minimizing the sum S,

$$S = \sum_{i=1}^{6} [y(\lambda_i) - \epsilon(r,R)\, N(T,\lambda_i)]/w_i, \qquad (4)$$

where $y(\lambda_i)$ is the measured spectral radiance at ith pyrometer wavelength λ_i, $N(T,\lambda_i)$ is the Planck black-body spectral radiance, T is the shock temperature, $\epsilon(r,R)$ is the emissivity that depends on the reflectivities of the shock front r and

TABLE VII. Summary of MgO shock T data. Numbers in parentheses are 1σ uncertainties for the last significant digit(s). ΔT_1 and ΔT_2 are the temperature correction factors for 1% increase of (1) light intensity recorded by the shock pyrometer and (2) reflectivity of the shock front (0.02 to 0.03 or 0.22 to 0.23), respectively.

	P (GPa)		T (kK)		ΔT_1 (K)		ΔT_2 (K)	
Shot	Exper.	Our EOS	$r = 0.02$	$r = 0.22$	$r = 0.02$	$r = 0.22$	$r = 0.02$	$r = 0.22$
390	102(1)	102(1)	3.91(10)	4.06(10)	6.0	6.6	4.9	7.7
387	106(2)	107(2)	3.88(10)	4.03(10)	5.6	6.2	4.4	7.1
389	124(1)	124(1)	4.53(10)	4.71(10)	7.7	8.4	6.9	10.1
384	158(2)	159(2)	5.4(3)	5.6(3)	12.2	13.4	10.4	15.2
383	173(3)	176(3)	6.0(3)	6.3(3)	14.8	16.3	13.2	19.0
391	203(1)	203(1)	7.0(2)	7.4(2)	20.2	22.6	18.9	27.1
405	221(1)	220(1)	7.7(3)	8.2(3)	23.7	26.7	22.2	32.2
406	220(3)	220(3)	7.9(3)	8.2(3)	25.3	27.3	14.0	20.9
410	247(2)	248(2)	8.5(3)	9.1(3)	28.0	31.9	26.3	38.3
411	248(3)	248(3)	8.7(3)	9.1(3)	29.4	31.9	16.2	24.4

MgO-vacuum interface R, and w_i is the weight assigned to the ith spectral radiance channel. For the unweighted fits, all $w_i = 1$. For the weighted fits, we used the estimated precision of the ith data point, as suggested in Ref. [86],

$$w_i = y(\lambda_i)^2\,[(dV_i/V_i)^2 + (dV_{0i}/V_{0i})^2], \tag{5}$$

where V_{0i} and V_i are pyrometer output signals recorded respectively by the ith channel during the calibration and actual shock experiment, and dV indicates the RMS noise over the selected portion of the radiance recording window. The measured value of spectral radiance at the ith pyrometer wavelength is

$$y(\lambda_i) = \mathrm{rad}_i \frac{V_i \mathrm{cor}_i}{V_{0i}}, \tag{6}$$

where rad_i is the spectral radiance of the calibration source at ith wavelength and cor_i is the correction factor, in general, time- and wavelength-dependent, for the ith pyrometer channel. This correction includes the difference of photodetector response to long (calibration) and short (actual shock T measurement) pulses, degradation of the front surface turning mirror, and wavelength-dependent transmittance of the gray filter installed after calibration in some high-temperature experiments. Each of these terms in the correction factor was determined by suitable measurements.

The emissivity ϵ_1 for the unwindowed configuration is

$$\epsilon_1 = \frac{(1-R)(1-r)}{(1-Rr)}, \tag{7}$$

whereas the emissivity ϵ_2 for the windowed configuration is

$$\epsilon_2 = \frac{\epsilon_1\, T_w}{1-(1-\epsilon_1)(1-T_w)}, \tag{8}$$

where T_w is the overall transmittance of the stack of sapphire windows. Evidently, $\epsilon_2 = \epsilon_1$ for $T_w = 1$.

We also evaluated the temperature uncertainty for each experiment and compared the measured values with the results of our model predictions. For shock T calculations along the Hugoniot [51–53] for MgO with initial T of 1850 K we used the Mie-Grüneisen EOS with the maximum likelihood estimates for the D versus U, $\gamma = \gamma_0\, V/V_0$ model with $\gamma_0 = 1.43 \pm 0.04$ and the Debye model for the specific heat with Debye temperature of 806 K at the ambient reference volume [71].

Only two experiments, 407 and 408 (see Sec. I A of Ref. [33]), yielded temperatures quite different from the model predictions, whether with unweighted or weighted fits for shock temperature alone or for both shock temperature and emissivity. They also exhibited a profound inconsistency between brightness and color temperatures. As seen in Fig. 6, 407 is the only shot (except for 391, which suffered from sample contamination by Ti evaporation) with a large ramp towards higher brightness temperature during the shock transit time. We speculated that experiment 407 might have suffered from a different transient response of the photodetectors caused by a combination of lower electrical load (no backup scope channels connected in parallel) and higher signal level (800–900 mV versus 300–700 mV in most other experiments). However, tests of the response of all our photodetectors up to 1.1 V output voltage did not affect the rate of "brightening" [26]. Either the gold mirror used to monitor the preheating temperature or the expendable silver mirror that sends light to the six-channel pyrometer may have performed differently in this particular experiment, but it is difficult to see how this would explain an unusually high longitudinal thermal gradient or anomalous ramp in input optical signals or electronic output levels. There is always a slight chance for the phototodetectors to pick-up some electrical noise from the RF-heater operating at high voltage, especially when the heating coil breaks. Although the level of such cross-talk and its potential impact on our measurements cannot be tested in any configuration other than the actual shock experiment, we believe this was the most probable cause of data corruption in shot 407.

Experiment 408, as discussed in Sec. I A of Ref. [33], most probably suffered from misalignment of the silver turning mirror. The difference between our model predictions for MgO shock T and the measured values was +850 K for shot 407 and −2760 K for shot 408. These values correspond to $+2.83\sigma$ and -6.9σ deviations from the model or 0.0047 and 5.2×10^{-12} respective probabilities for these data to be observed in case of normal error distribution statistics. This is equivalent to 0.0564 and 6.24×10^{-11} expected events,

respectively, with such deviations from the model values in a sample of 12 measurements. Both numbers are much less than 0.5, the widely accepted threshold for statistical rejection of potentially bad data by Chauvenet's criterion [87]. Based on this criterion and the reasons discussed above, temperatures from these shots were excluded from further consideration.

B. Shock front reflectivity measurements and analysis

MgO shock front reflectivity was measured with the high-temperature semitransparent mirror technique [27]. Our method evolved from the technique that was independently proposed and applied to experiments with shocked CCl_4 by one of us in 1997 [88]. In turn, it was a modification of the original photometric method employing a solid metallic mirror and a streak camera first developed and applied for measurements in ionic crystals [89] and liquid krypton [90] at the Russian Federal Nuclear Center. There are several reports from other research fields on surface reflectivity or emissivity measurements [91,92] that employed semitransparent mirrors or beam splitters in a configuration similar to one we adopted for shock pyrometry.

Unlike the dynamic reflectivity method proposed recently by LaLone *et al.* [93], our technique does not require any external source of light and our method probes reflectivity at the same wavelengths and in the same geometry as used for temperature measurement. The procedure to determine the shock front reflectivity r from a pair of unwindowed and windowed shots at the same impact velocity is to vary r from its initial value of 2% until the temperature from the unwindowed shot analyzed with emissivity ϵ_1 [Eq. (7)] matches the temperature from the windowed shot analyzed with emissivity ϵ_2 [Eq. (8)].

The preliminary results reported in Ref. [27] were obtained from the analysis of radiance data at a common value of MgO thickness, ≈1.5 mm, for each pair of matching unwindowed and windowed shots. However, recalculating shock temperatures half-way between the driver plate and free surface was found not to be accurate enough for a reliable estimate of shock front reflectivity using this method. Hence we developed a more robust procedure for shock reflectivity extraction than that previously employed. From careful analysis of the raw radiance histories and temperature versus time profiles, we found the shape of every curve from the unwindowed shot nearly identical to its counterpart from the windowed shot. That allowed us to use the whole steady portion of time-dependent temperature profiles from the windowed shots for matching the data from their unwindowed counterparts via the same procedure of varying r.

Weighted temperature fits from shots 405 and 406 for shock reflectivities of 0.02 (brightness T) and 0.22 (true T) are shown for comparison in Fig. 7. The brightness temperature from windowed shot 406 is noticeably higher than that from unwindowed shot 405, as it should be for a reflective shock front. Both temperature profiles closely match for the value of $r = 0.22 \pm 0.04$. As evident from Fig. 7, the shapes of true temperature profiles from both experiments match over the entire overlap region with high accuracy. A counter-example showing the comparison of windowed and unwindowed shots

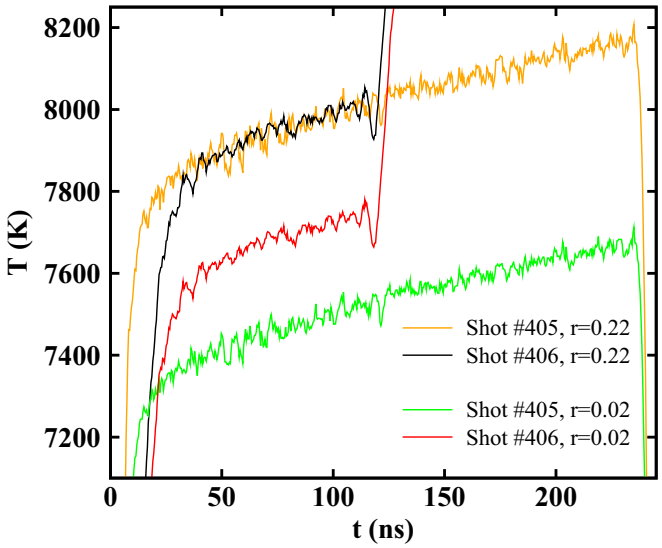

FIG. 7. Brightness and true temperature profiles from shots 405 and 406 done with the same pyrometer settings and at nearly the same impact velocity. The noise on records indicates the level of data precision. The brightness temperature from the windowed shot 406 is about 200 K higher than that from its unwindowed counterpart 405. Both temperature profiles match over the overlapped useful portions of both records at a shock front reflectivity value of $r = 0.22 \pm 0.04$.

with an unreflective shock front in Mg_2SiO_4 forsterite at ≈210 GPa can be found in Sec. IV of Ref. [33].

The pair of shots 410 and 411 gave a similar result for the optical reflectivity of the shock front, $r = 0.21 \pm 0.04$ (Fig. 8). The uncertainty of reflectivity, ±0.04, for both pairs of matched experiments, translates into a 5% contribution to

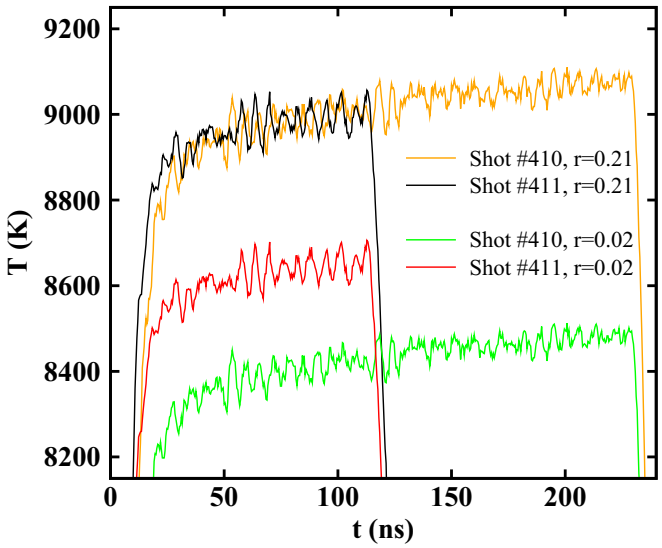

FIG. 8. Brightness and true temperature profiles from shots 410 and 411 done with the same pyrometer settings and at nearly the same impact velocity. The noise on records indicates the level of data precision. The brightness temperature from the windowed shot 411 is about 200 K higher than that from its unwindowed counterpart 410. Both temperature profiles match over the overlapped useful portions of both records at shock front reflectivity value of $r = 0.21 \pm 0.04$.

the uncertainty in the absolute radiance and hence an ≈1% contribution to the true temperature determination.

Our values of MgO shock reflectivity along the preheated Hugoniot at 220–250 GPa and approximately 8000−9000 K are substantially higher than those along the room-T Hugoniot at either equal pressure (but ≈4000 K lower temperature) or at equal temperature (but ≈100 GPa higher pressure). On the principal Hugoniot from 174 to 203 GPa and 3000–4000 K, shock reflectivity has not been measured but low values are demonstrated by reasonably good agreement between the experimental shock T data and model predictions with $r = 0$ [25] or our EOS with $r = 0.02$ [26]. In decaying laser shock experiments, ≈500 GPa is the lower limit at which shock reflectivity was detected at the <0.5% level from the analysis of VISAR fringe intensities for polarized coherent light at a single wavelength [22] or two wavelengths [23]. Root *et al.* also noted a transition from essentially nonreflecting shocks in MgO at ≈270 GPa to somewhat reflecting shocks at some unspecified higher pressure but did not publish quantitative reflectivity results despite the superior quality of their multipoint VISAR data [18]. No measurable shock front reflectivity data were reported by McWilliams *et al.* [22] or Bolis *et al.* [23] at approximately 8000–9000 K shock T, which is reached along the principal Hugoniot at approximately 350–360 GPa, some 100 GPa higher than our data points at equal temperature. The absence of phase transitions below ≈360 GPa [18] and continuity of data suggest low values of MgO shock reflectivity everywhere along the principal Hugoniot up to ≈500 GPa. In this context, it is interesting that we obtain a much better match between the shock T model predictions on the 1850-K Hugoniot and the results of our measurements at approximately 100 GPa when we perform our spectral radiance data analysis with reflectivity $r = 0.22$, as suggested by our direct reflectivity measurements at 220–250 GPa, rather than $r = 0.02$.

These observations deserve several comments. First, our technique for measuring shock front reflectivities is superior in accuracy and applicability to any measurements from VISAR signals because the latter employ coherent polarized light at one or two wavelengths only and require an additional *specular reflector* characterized for the absolute reflectivity [94]. Comparison of signals from the reference metal reflector (well aligned, perfectly flat diamond-turned surface) recorded *before* shock compression and those taken from the moving shock front (with some tilt and nonplanarity) *during* the shock compression can easily lead to large errors. In contrast, our method compares two very similar sources of thermal radiation (or nearly *Lambertian emitters*) at virtually the same experimental conditions. Our technique has much less stringent requirements for the alignment and absolute intensity calibration than the conventional specular VISAR reflectometry discussed above. Second, our reflectivity data, though different from those seen or inferred for MgO at other conditions, are exactly the same as those measured in shocked diamond just slightly below its melt line [95]. Third, our data from shock reflectivity measurements in molten MgO [96] appear to be almost identical to those reported here.

The results of *ab initio* molecular dynamics simulations by Qi *et al.* suggest that shock front reflectivities in quartz and fused silica compressed up to approximately 2 TPa and 10^5 K are more dependent on temperature than pressure [97]. Although high reflectivities are often typical of molten substances, we see no evidence of MgO melting up to the highest pressure studied along the 1850-K Hugoniot.

V. MAXIMUM DEGREE OF MGO SUPERHEATING IN OUR EXPERIMENTS

A. Features of well studied shock-induced phase transitions

There are widespread reports in the literature of large degrees of superheating of shock-compressed solids before melting [98], which suggests the possibility that our temperature observations in MgO do not provide a meaningful measurement of the equilibrium melting curve. However, we show here via a systematic review of superheating claims that these observations have been universally misinterpreted. Superheating occurs only under very specific circumstances that do not apply to the direct shock melting of B1 MgO.

1. Lack of temperature reversal on pressure decay in shock-melted diamond, B2 phase MgO, stishovite, and B1 phase MgO

To the best of our knowledge, there are no published data that constrain whether superheating of B1 phase MgO, specifically, occurs before melting during shock compression. However, observations of a decaying shock wave passing from liquid shock states downwards into the high-pressure solid B2 phase show no temperature reversal [22]. In this regard, the temperature behavior at the B2 MgO shock melting point is similar to observations of shock melting of diamond [99] and crystalline stishovite [19]. The relation between shock T and P observed in these studies resembles all (in the case of stishovite) or a portion of (in the case of diamond) the typical three-segment curves first determined experimentally for shocked alkali halides [100,101]. Neither substance exhibits superheating upon melting [19,99]. Our B1-phase MgO melting data from 2300-K experiments [96] show the same features as diamond or crystalline stishovite: monotonic increase of shock temperature versus peak pressure (discrete data) and monotonic decrease of light intensity as a longitudinal release wave overtakes and attenuates a shock front (continuous data). The shape of time-resolved radiance histories from our samples compressed to the solid-liquid coexistence line look very similar to those from the solid samples shown in Ref. [27].

2. Temperature reversal observed at B2-B1 solid-solid phase transformation in MgO compressed by decaying shocks

As discussed above in Sec. I, the reversal of temperature or, more correctly, of light intensity emitted by MgO during compression by decaying laser shocks was attributed to the B2 to B1 solid-solid phase transformation [22]. If this interpretation is correct, it demonstrates that crystal structure can change rapidly (within a few nanoseconds) and alter the shock temperature and optical properties of initially transparent and uniform B1 phase. Since there is a significant (≈5%) volume collapse during the B1-B2 transition [18], it must be accompanied by splitting of a single shock into a double-wave profile upon dynamic compression. Unfortunately, these time-dependent wave profiles were never actually measured for

MgO [18,21,22], leading to substantial uncertainty in pressure determination above the solid-solid transition. Furthermore, shocking solid 298-K MgO to 270 GPa or higher causes substantial light scattering [18], which reduces the apparent emissivity of the samples [102], and leads to large uncertainty in temperature measurements. In turn, this makes determination of the phase boundary slope $d\mathrm{P}/dT$ (and the entropy change of the B1-B2 transition) very uncertain. This explains the lack of reproducibility of the phase boundary slope in three experiments by Bolis *et al.* [23] and the much higher value of $d\mathrm{P}/dT$ (and unrealistically high entropy increase) inferred by McWilliams *et al.* [22]. Part of the problem may be instrumental: if the time resolution of streaked optical pyrometers in these studies (presumably a function of streak rate and hence of laser intensity) was not high enough to resolve the fast jump in optical emission as the shock decayed, that would by itself yield an artificially large value for $d\mathrm{P}/dT$.

3. Similar shape of the melting curves of laser heated GaAs in superheated and equilibrium molten states

Unfortunately, the observation of a traditional three-segment curve for the T versus P—with a low-slope mixed-phase segment separating compression of pure solid and pure liquid phases—is not sufficient evidence for the absence of superheating. For example, experiments on GaAs heated from ambient conditions by 10 ns or by 25 ps laser pulses showed a three-segment behavior with a well-defined plateau in the surface T versus normalized laser fluence curve, despite 500 to 600 K superheating (with $\Delta T_m/T_m \approx 0.3$–$0.4$) [103]. Therefore a direct comparison of our (P,T) data with the predicted melting curves for MgO requires accurate assessment of the potential for B1 solid phase superheating in our experiments.

Since the static melting temperature extrapolations and computational predictions for MgO above ≈135 GPa differ by ≈3000 K (see Fig. 1), the equilibrium melting curve of MgO cannot by itself tell us whether our shock temperatures indicate superheating or not. Indeed, that was the motivation to do these experiments. Instead, we must reason by analogy and estimate the potential degree of superheating upon shock melting of B1 phase MgO with reference to the melting behavior of those substances with properties similar to MgO whose static and dynamic melting behaviors are both well-studied: SiO_2 (fused silica, quartz, and stishovite) [19,104–109], Mg_2SiO_4 forsterite [106,110], and single-crystal aluminum [111,112].

4. Melting of superheated and crystallization of supercooled shock-compressed aluminum

The results of accurate MD simulations of shock melting in ideal single-crystal aluminum [111] show that uniaxial compression along ⟨100⟩ is the most favorable for superheating because it generates minimum shear stress. In turn, a shock in this orientation creates the smallest number of defects and dislocations that may act as nucleation sites for the liquid phase. Such defects change the mechanism of melt nucleation from homogeneous to heterogeneous. This consideration is equally valid for any fcc crystal, including B1 phase MgO.

The simulations of Budzevich *et al.* [111] yield a maximum superheating temperature $\Delta T_m = 583$ K for an ideal aluminum crystal shocked along ⟨100⟩, which completely relaxes to the equilibrium melting temperature $T_m = 3420$ K in ≈40 ps. This degree of superheating, $\Delta T_m/T_m \approx 0.17$, is similar to analytical predictions using the homogeneous nucleation theory for Al heated from ambient conditions either at the surface by ultrashort laser pulses [112] or throughout the volume by high electric current [113,114]. Consideration of the density of screw and edge dislocations in real aluminum crystals lowers the maximum degree of superheating for the case of quasisteady volumetric heating from ambient conditions by about a factor of two, from ≈0.21 to ≈0.12 [114,115]. Although these results show that melting of cubic solids shocked along ⟨100⟩ directly from their initial phases may result in superheating up to approximately 500–1000 K, this has never been observed in practice because the duration of the excess temperature pulse is much too short to be observed with current shock diagnostic technology.

For aluminum shocked along ⟨110⟩ and ⟨111⟩ directions, the authors of Ref. [111] obtained, rather than superheating, the opposite phenomenon of metastable cold melts lying ≈700 K below the equilibrium melting curve of aluminum. The metastable cold melt completely recrystallized within ≈20 ps and thermal relaxation took less than ≈53 ps. The degree of supercooling in these simulations, approximately 0.31 at 61 GPa [111], is similar to the value of ≈0.36 obtained via multiscale MD simulations of the formation of stishovite during shock compression of quartz and fused silica [116].

5. Supercooling of shock-melted quartz and fused silica

Metastable states in shock-compressed quartz and fused silica have been inferred by several groups on the basis of nonmonotonic trends in discrete (shock T versus P) [104–108] or continuous (emitted radiant power versus time for decaying shocks) [104,105,108,109] data. Recent decaying laser shock experiments by Millot *et al.* confirmed the anomalous response of quartz and fused silica but revealed no metastable states in directly shocked synthetic stishovite [19]. This difference was unexpected because both shocked quartz and fused silica are known to transform to stishovite prior to melting [117].

This paradox in observations was resolved by recent findings of Gleason *et al.* [118] and Shen *et al.* [116]. The first group experimentally observed crystallization of stishovite on an ≈1.4-ns time scale during shock compression of fused silica. The second group performed multiscale MD simulations that revealed fast (10 ps) formation of a metastable disordered state (cold melt) followed by slow (from 1.5 to 5 ns or even more) crystallization of stishovite from shock-compressed quartz and fused silica via homogeneous nucleation and grain growth [116]. The results of these simulations (Ref. [116(a)], Fig. 5) are qualitatively the same as those for shocked ⟨110⟩ and ⟨111⟩ aluminum (Sec. V A 4). The only difference is recrystallization of shocked Al into the same starting fcc phase versus crystallization of new stishovite phase in shocked quartz or fused silica at later stages of compression. The estimated time scale for stishovite crystallization, approximately 1.5 ns [116], is ≈2 times longer than the fastest rise time of reported temperature reversals (see Fig. S8 of the Supplement to Ref. [19]).

While the predicted pressure for the shock T anomaly is approximately 5–10 GPa lower than the experimental value of ≈72 GPa for fused silica and approximately 25 GPa lower than the reported ≈110 GPa for quartz [105,116], the simulation results (Ref. [116(a)], Fig. 5) show a much better agreement with the measurements of the highest pressure at which the solid stishovite phase is stable during shock compression: 63.3 GPa for fused silica and 91.5 GPa for quartz [105]. The same type of measurements done near both points of shock T anomaly always yielded noticeably lower sound speeds than those expected for pure crystalline stishovite [105].

It appears that all the reported nonmonotonic behaviors in quartz and fused silica [19,104–109] are manifestations of supercooling, not of superheating. This is the only explanation consistent with the comparison between simulated [116] and experimental shock temperature [19,106,108,109] or sound speed data [105] for quartz and fused silica and the results of melting curve predictions [119,120] for SiO_2 from 20 to 160 GPa from MD simulations employing potentials sufficiently accurate to reproduce the boundaries between several solid phases.

6. Non-monotonic T versus P in shocked forsterite

Superheating of forsterite [98] was inferred from comparison of data on two different minerals: (1) pure synthetic single-crystal Mg_2SiO_4 [106,107] and (2) natural peridot $(Mg_{0.9},Fe_{0.1})_2SiO_4$ [110]. This solution was adopted because it was thought that the emissivity of synthetic forsterite in the melting range is too low for effective pyrometry [110], but the apparent result is that forsterite is the only substance believed to show an enormous, ≈2700 K, drop in shock T between a superheated solid state at 127 GPa and a molten state at 133 GPa [98]. This value corresponds to $\Delta T_m/T_m \approx 0.63$ and a normalized energy barrier of approximately 20, which is 3 to 16 times higher than that for any other substance [98].

We recently measured shock temperature in pure synthetic single-crystal Mg_2SiO_4 samples in the same pressure range as the earlier natural peridot measurements [121] using the improved Caltech six-channel pyrometer calibration [26]. We found a decrease in light intensity in shocked forsterite between ≈120 GPa and higher pressures equivalent to a temperature drop of ≈1000 K. Intense time-dependent scattering at short pyrometer wavelengths (500–600 nm) in this experiment, similar to that observed by Lyzenga at ≈140 GPa [107], indicates that the true temperatures above the phase transition are higher than those inferred from pyrometry data when this effect is neglected. Therefore the actual temperature decrease is $<$ 1000 K and the observation of a temperature minimum along the Hugoniot may be an artifact of this type of measurement. Our pyrometry data at that point also indicate a double-wave structure [121] typical of solid-solid phase transitions with fast volume collapse. It is generally accepted that forsterite is metastable above ≈25 GPa and under shock it may recrystallize to a denser form or decompose into MgO and $MgSiO_3$. Even at ≈210 GPa, where we observe a slow (≈150-ns) decrease of shock T [121], this may indicate that phase transformation to melt is not yet complete. Our interpretation is that the observed temperature drop above ≈120 GPa is not, as commonly interpreted, due to overheating of a solid substance followed by catastrophic melting. Rather it indicates time-dependent transformation via incongruent nucleation and growth, with at least one solid phase preserved.

B. Superheating requires incongruent shock melting or recrystallization

To summarize our review of the reproducible nonmonotonic behavior of shock T versus P in SiO_2 and Mg_2SiO_4, we conclude that in neither substance is this due to superheating of solid phases followed by congruent melting. Rather, all the nonequilibrium phenomena observed in the temperature of dynamically compressed solids are caused by the kinetics of either solid-solid transformations or the conversion of starting materials to additional metastable solid phases before shock melting. In other words, deviation from a monotonic relation between shock T and P, whether observed in discrete steady shocks or in continuous recording of decaying shocks, requires formation of at least one new solid phase, different from the phase of the starting solid material. We find no exception to this rule and so we argue that none of the emitted light reversals observed in decaying shocks are sufficient to claim superheating at the melting line.

Superheating can only be unambiguously identified and quantified by direct comparison of reliable melting data from static and shock measurements at equal pressure. Such comparisons have been done, for example, for NaCl [122] and bismuth [123]. Shock melting data of Kormer for NaCl [100,101] appear to plot only approximately 140–190 K above the melt line of Boehler [122], well within the uncertainty level of the shock T data alone. In the case of CsI, the attribution of an emitted light intensity reversal in shock melted CsI to superheating by the authors [124] is clearly disproved by direct comparison of the shock and the static melting curve measurements [124,125].

Finally, in the case of Bi, recent femtosecond x-ray diffraction results put an upper limit of 3 ns on the melting time of polycrystalline Bi during release from a shocked state to 14 GPa and confirm that there is no detectable superheating [123]. Complete melting of a highly superheated metal crystal with $\Delta T_m/T_m \approx 0.5$ will take less than a picosecond [112]. Likewise, Kormer and coworkers used refractive index measurements at and behind the shock front to show that melting of initially transparent alkali halides takes $<$10 ps to complete [126]. It is therefore, we argue, extraordinarily unlikely that shocked B1 MgO could radiate at a temperature nearly twice as high as the melting curve for over 20 ns (the shortest time needed for the samples in our experiments to become completely opaque). That would be a melting time orders of magnitude longer than documented in any alkali halide at a degree of superheating higher than any observed. Therefore we are confident that the level of superheating that may have occurred in our experiments is less than or equal to the 1σ uncertainty of the measured true shock T. When we compare our (P,T) data with the proposed candidate melting curves (Fig. 9), we therefore eliminate with confidence the curves of Zerr and Boehler [1], Aguado and Madden [11], Strachan *et al.* [8], Belonoshko [14], and Yoshimoto [15] because our temperature at 248 GPa exceeds their curves by 1300 to 3300 K, much more than our uncertainty.

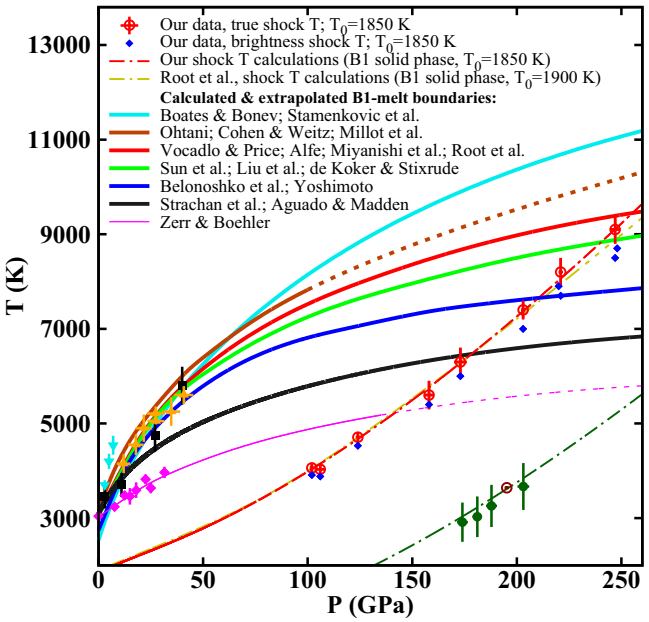

FIG. 9. Summary of our shock temperature data from MgO preheated to 1850 K, the reported melting data [1–20] and conventional shock temperature data [25,26]. All unlabeled data are the same as those shown in Fig. 1. Typical uncertainties of the predicted melt lines are 100–200 K. Thicker lines indicate several melting curves that are close enough to be grouped and shown together. Dashed lines are the results of our numerical extrapolation of the reported data. All crosses are the actual error bars.

VI. SUMMARY

The Hugoniot and radiative temperature data for a single-crystal MgO preheated to 1850 K and shock compressed along ⟨100⟩ to the previously unsampled range of $P-T$ from 102 GPa and 3900 K to 248 GPa and 9100 K are reported. The uncertainties of the majority of the primary experimental data points do not exceed 1%–2% for the Hugoniot parameters and 3%–4% for the final true temperature.

Shock front reflectivity was measured at 220 and 248 GPa, yielding consistent values of 0.22 ± 0.04 and 0.21 ± 0.04, respectively. Such high reflectivities indicate considerable ionization, often seen in molten substances. The reflectivity may be an indicator of premelting phenomena and close approach to the MgO melting boundary in these high-pressure shock states. However, no other evidence of melting was detected in the Hugoniot or shock temperature data from this series of experiments.

Accurate families of Hugoniots were constructed, by review of all available data with their uncertainties and application of state-of-the-art methods of general least-squares fitting. We present Hugoniots for MgO with initial temperatures of 298, 1850, and 2300 K and a parametrization of the Hugoniot as a function of initial temperature valid from 298 to 2400 K.

Our maximum likelihood solutions allow us to evaluate popular models for the volume dependence of the Grüneisen parameter and to constrain ambient Grüneisen coefficients for MgO with the highest accuracy permitted by the selected models and quality of available experimental data. These results were validated by (1) the good agreement between our Grüneisen data and five semiempirical $\gamma(V)$ models calibrated by porous shock data only or by combined static and shock data sets and (2) the very good agreement between our 1-bar Grüneisen values and $\gamma(T)$ at ambient pressure recalculated from reported experimental data on the adiabatic bulk modulus $K_s(T)$.

The EOS for the B1 phase of MgO with $\gamma = \gamma_0 V/V_0$ and $\gamma_0 = 1.43 \pm 0.04$ was used to predict shock temperatures for the conditions of our experiments. For the whole range of pressures examined here, there was a very good agreement between the results of our predictions, experimental true shock temperature values, and the results of QMD simulations reported by Root *et al.* [18]

Our brightness and true temperature data are compared to literature values and computational predictions of the melting curve of B1 MgO in Fig. 9. Our highest temperature datum at 248 GPa and 9100 K, which we consider to remain in the solid B1 phase, exceeds the melting curves of Zerr and Boehler [1], Aguado and Madden [11], Strachan *et al.* [8], Belonoshko [14], and Yoshimoto [15] by 1300 to 3300 K. As of today, this level of superheating has never been reliably observed in shock-compression experiments probing congruent melting of the starting phase. We conclude that such extreme superheating of melts on the time scales of these large-sample shock experiments is very unlikely to occur and submit that our results provide a lower bound on the melting curve of MgO well above these lowest candidate melting curves.

ACKNOWLEDGMENTS

Technical staff members of the Caltech Lindhurst Laboratory of Experimental Geophysics Michael Long, Epaprodito Gelle, and Russel Oliver are gratefully acknowledged for their expert assistance with all experiments. We thank our LLNL collaborators Samuel Weaver and Paul Benevento for sharing their extensive knowledge about successful operating of two-stage light-gas guns beyond 7 km/s and for providing the projectiles for our experiments 408–411. OVF thanks Prof. I. V. Lomonosov of IPCP RAS, Russia for giving access to the unpublished thermodynamic data for MgO predicted by the wide-range semiempirical EOS. This work was supported by the U.S. NSF, Award Nos. EAR-0810116 and EAR-1426526.

[1] A. Zerr and R. Boehler, Nature (London) **371**, 506 (1994).
[2] L. Zhang and Y. Fei, Geophys. Res. Lett. **35**, L13302 (2008).
[3] Z. Du and K. K. M. Lee, Geophys. Res. Lett. **41**, 8061 (2014).
[4] T. Kimura, H. Ohfuji, M. Nishi, and T. Irifune, Nat. Commun. **8**, 15735 (2017).
[5] E. Ohtani, Phys. Earth Planet. Inter. **33**, 12 (1983).
[6] L. Vočadlo and G. D. Price, Phys. Chem. Miner. **23**, 42 (1996).
[7] R. E. Cohen and J. S. Weitz, in *Properties of Earth and Planetary Materials at High Pressure and Temperature*, edited by M. H. Manghnani and T. Yagi, Geophysical Monograph Series 101 (American Geophysical Union, Washington, DC, 1998), pp. 185–196, available at http://onlinelibrary.wiley.com/doi/10.1029/GM101p0185/summary; arXiv:mtrl-th/9605001.

[8] A. Strachan, T. Çağin, and W. A. Goddard III, Phys. Rev. B **60**, 15084 (1999).

[9] D. Alfè, Phys. Rev. Lett. **94**, 235701 (2005).

[10] X. W. Sun, Q. F. Chen, Y. D. Chu, and C. W. Wang, Physica B **370**, 186 (2005).

[11] A. Aguado and P. A. Madden, Phys. Rev. Lett. **94**, 068501 (2005).

[12] Z. J. Liu, X. W. Sun, Q. F. Chen, L. C. Cai, X. M. Tan, and X. D. Yang, Phys. Lett. A **353**, 221 (2006).

[13] N. de Koker and L. Stixrude, Geophys. J. Int. **178**, 162 (2009).

[14] A. B. Belonoshko, S. Arapan, R. Martonak, and A. Rosengren, Phys. Rev. B **81**, 054110 (2010).

[15] Y. Yoshimoto, J. Phys. Soc. Jpn. **79**, 034602 (2010).

[16] B. Boates and S. A. Bonev, Phys. Rev. Lett. **110**, 135504 (2013).

[17] K. Miyanishi, Y. Tange, N. Ozaki, T. Kimura, T. Sano, Y. Sakawa, T. Tsuchiya, and R. Kodama, Phys. Rev. E **92**, 023103 (2015).

[18] S. Root, L. Shulenburger, R. W. Lemke, D. H. Dolan, T. R. Mattsson, and M. P. Desjarlais, Phys. Rev. Lett. **115**, 198501 (2015).

[19] M. Millot, N. Dubrovinskaia, A. Černok, S. Blaha, L. Dubrovinsky, D. G. Braun, P. M. Celliers, G. W. Collins, J. H. Eggert, and R. Jeanloz, Science **347**, 418 (2015).

[20] V. Stamenković, D. Breuer, and T. Spohn, Icarus **216**, 572 (2016).

[21] R. Smith, J. K. Wicks, R. G. Kraus, J. Eggert, F. Coppari, M. Newman, M. A. Millot, and T. S. Duffy, *Crystal Structure of MgO Along the Shock Hugoniot*, EOS Transactions AGU 97 Fall Meeting Supplement, Abstract MR13B-06 (2016) available at http://adsabs.harvard.edu/abs/2016AGUFMMR13B..06S.

[22] R. S. McWilliams, D. K. Spaulding, J. H. Eggert, P. M. Celliers, D. G. Hicks, R. F. Smith, G. W. Collins, and R. Jeanloz, Science **338**, 1330 (2012).

[23] R. M. Bolis, G. Morard, T. Vinci, A. Ravasio, E. Bambrink, M. Guarguaglini, M. Koenig, R. Musella, F. Remus, J. Bouchet, N. Ozaki, K. Miyanishi, T. Sekine, Y. Sakawa, T. Sano, R. Kodama, F. Guyot, and A. Benuzzi-Mounaix, Geophys. Res. Lett. **43**, 9475 (2016).

[24] F. Coppari, R. F. Smith, J. H. Eggert, J. Wang, J. R. Rygg, A. Lazicki, J. A. Hawreliak, G. W. Collins, and T. S. Duffy, Nat. Geosci. **6**, 926 (2013).

[25] B. Svendsen and T. J. Ahrens, Geophys. J. Int. **91**, 667 (1987).

[26] O. V. Fat'yanov and P. D. Asimow, Rev. Sci. Instr. **86**, 101502 (2015).

[27] O. V. Fat'yanov and P. D. Asimow, J. Phys.: Conf. Ser. **500**, 062003 (2014).

[28] O. V. Fat'yanov, P. D. Asimow, and T. J. Ahrens, AIP Conf. Proc. **1195**, 855 (2009).

[29] D. E. Fratanduono, J. H. Eggert, M. C. Akin, R. Chau, and N. C. Holmes, J. Appl. Phys. **114**, 043518 (2013).

[30] O. V. Fat'yanov and P. D. Asimow, J. Appl. Phys. **121**, 115904 (2017).

[31] P. D. Asimow and T. J. Ahrens, J. Geophys. Res. **115**, B10209 (2010).

[32] S. C. Gupta, S. G. Love, and T. J. Ahrens, Earth Planet. Sci. Lett. **201**, 1 (2002).

[33] See Supplemental Material at http://link.aps.org/supplemental/10.1103/PhysRevB.97.024106 for further details of our experiments, data analysis, Grüneisen model validation, and the tabular data files, which also includes Refs. [34–43].

[34] V. Gospodinov, Int. J. Mod. Phys. B **28**, 1450196 (2014); arXiv:1401.1041.

[35] M. H. Rice, J. Phys. Chem. Solids **26**, 483 (1965).

[36] O. L. Anderson, J. Geophys. Res. **84**, 3537 (1979).

[37] S. K. Srivastava and P. Sinha, Physica B **404**, 4316 (2009).

[38] R. Jeanloz, J. Geophys. Res. **94**, 5873 (1989).

[39] A. V. Bushman, I. V. Lomonosov, V. E. Fortov, K. V. Khishchenko, M. V. Zhernokletov, and Yu. N. Sutulov, Zh. Eksp. Teor. Fiz. **109**, 1662 (1996) [JETP **82**, 895 (1996)]; K. V. Khishchenko, J. Phys.: Conf. Ser. **653**, 012081 (2015).

[40] F. D. Stacey and P. M. Davis, Phys. Earth Planet. Inter. **142**, 137 (2004).

[41] V. N. Zharkov, Phys. Earth Planet. Inter. **109**, 79 (1998).

[42] S. S. Kushwah and M. P. Sharma, Solid State Commun. **152**, 414 (2012).

[43] D. Zhang and J. X. Sun, Chin. Phys. B **21**, 080508 (2012).

[44] S. P. Marsh, *LASL Shock Hugoniot Data* (University of California Press, Berkeley, 1980).

[45] M. S. Vassiliou and T. J. Ahrens, Geophys. Res. Lett. **8**, 729 (1981).

[46] L. Zhang, Z. Gong, and Y. Fei, J. Phys. Chem. Solids **69**, 2344 (2008).

[47] G. D. Stevens, L. R. Veeser, P. A. Rigg, and R. S. Hixson, AIP Conf. Proc. **845**, 1353 (2006).

[48] A. C. Mitchell and W. J. Nellis, J. Appl. Phys. **52**, 3363 (1981).

[49] R. K. Böck, *Application of a Generalized Method of Least Squares for Kinematical Analysis of Tracks of Bubble Chamber Photographs*, CERN 60-30 (CERN, Geneva, 1960), available at http://dx.doi.org/10.5170/CERN-1960-030.

[50] S. Brandt, in *Statistical and Computational Methods in Data Analysis*, 1st ed. (North-Holland, Amsterdam, 1970), p. 181; typos corrected in the 4th ed. (Springer International, Switzerland, 2014), p. 251.

[51] J. M. Walsh and R. H. Christian, Phys. Rev. **97**, 1544 (1955); The first reported use of constant $b = (\partial P/\partial T)_v/C_v$, which is just another form of γ/V function.

[52] J. Wackerle, J. Appl. Phys. **33**, 922 (1962).

[53] R. G. McQueen, J. N. Fritz, and S. P. Marsh, J. Geophys. Res. **69**, 2947 (1964); R. G. McQueen, S. P. Marsh, and J. N. Fritz, *ibid.* **72**, 4999 (1967).

[54] L. V. Al'tshuler, S. E. Brusnikin, and E. A. Kuz'menkov, Zh. Prik. Mekh. Tekhn. Fiz. **1**, 134 (1987) [J. Appl. Mech. Tech. Phys. **28**, 129 (1987)].

[55] A. M. Molodets, Fizika Goreniya i Vzryva **31**, 132 (1995) [Combustion, Explosion and Shock Waves **31**, 620 (1995)].

[56] A. M. Molodets, Fizika Goreniya i Vzryva **42**, 110 (2006) [Combustion, Explosion and Shock Waves **42**, 346 (2006)]; Slopes and intercepts of 1850-K MgO Hugoniot were calculated from the reported there parameters and equations.

[57] S. K. Saxena and G. Sheng, J. Geophys. Res. **97**, 19813 (1992).

[58] M. W. Chase, Jr., in *NIST-JANAF Thermochemical Tables*, 4th ed., J. Phys. Chem. Ref. Data, Monograph 9 (National Institute of Standards and Technology, Gaithersburg, MD, 1998), p. 1536, available from NIST archive at https://srd.nist.gov/JPCRD/jpcrdM9.pdf.

[59] K. Wang and R. R. Reeber, in *Computer-Aided Design of High-Temperature Materials*, edited by A. Pechenik, R. K. Kalia, and P. Vashishta (Oxford University Press, New York, 1999), p. 473.

[60] M. H. G. Jacobs and H. A. J. Oonk, Calphad **24**, 133 (2000); Phys. Chem. Chem. Phys. **2**, 2641 (2000); S. Raju, E. Mohandasa, and K. Sivasubramanian, *ibid.* **3**, 1391 (2001).

[61] L. S. Dubrovinsky and S. K. Saxena, Phys. Chem. Miner. **24**, 547 (1997).

[62] G. Fiquet, P. Richet, and G. Montagnac, Phys. Chem. Miner. **27**, 103 (1999).

[63] P. D. Asimow, D. Sun, and T. J. Ahrens, Phys. Earth Planet. Inter. **174**, 302 (2009).

[64] A. B. Medvedev and R. F. Trunin, Phys.-Usp. **182**, 829 (2012) [Phys.-Ups. **55**, 773 (2012)].

[65] D. Grady, G. Fenton, and T. Vogler, J. Phys.: Conf. Ser. **500**, 152007 (2014).

[66] J. Hama and K. Suito, Phys. Earth Planet. Inter. **114**, 165 (1999).

[67] G. H. Miller, T. J. Ahrens, and E. M. Stolper, J. Appl. Phys. **63**, 4469 (1988).

[68] T. S. Duffy and T. J. Ahrens, J. Appl. Phys. **76**, 835 (1994).

[69] E. S. Zouboulis and M. Grimsditch, J. Geophys. Res. **96**, 4167 (1991).

[70] Y. Sumino, O. L. Anderson, and I. Suzuki, Phys. Chem. Miner. **9**, 38 (1983).

[71] D. G. Isaak, O. L. Anderson, and T. Goto, Phys. Chem. Miner. **16**, 704 (1989).

[72] S. Spetziale, C. S. Zha, T. S. Duffy, R. J. Hemley, and H. K. Mao, J. Geophys. Res. **106**, 515 (2001).

[73] B. L. N. Kennett and I. Jackson, Phys. Earth Planet. Inter. **176**, 98 (2009);

[74] Y. Tange, Y. Nishihara, and T. Tsuchiya, J. Geophys. Res. **114**, B03208 (2009); **115**, B12203 (2010).

[75] Y. Aizawa and A. Yoneda, Phys. Earth Planet. Inter. **155**, 87 (2006).

[76] W. J. Carter, S. P. Marsh, J. N. Fritz, and R. G. McQueen, in *Accurate Characterization of the High-Pressure Environments*, edited by C. Lloyd, Spec. Publ., 326E (National Bureau of Standards, Washington, DC, 1971), pp. 147–158, available at https://archive.org/download/accuratecharacte326lloy/accuratecharacte326lloy.pdf.

[77] L. V. Al'tshuler and I. I. Sharipdzhanov, Izv. Akad. Nauk SSSR, Fiz. Zem. **3**, 11 (1971) [Izv. Acad. Sci. USSR, Earth Phys. **3**, 167 (1971)].

[78] Caloric EOS description: I. V. Lomonosov, A. V. Bushman, V. E. Fortov, and K. V. Khishenko, AIP Conf. Proc. **309**, 133 (1994); Shock-wave database info: P. R. Levashov, K. V. Khishenko, I. V. Lomonosov, and V. E. Fortov, *ibid.* **706**, 87 (2004); Primary input experimental data are available at: http://www.ihed.ras.ru/rusbank/substsearch.php

[79] M. H. G. Jacobs and H. W. S. de Jong, Phys. Chem. Chem. Phys. **5**, 2056 (2003).

[80] P. I. Dorogokupets and A. Dewaele, High Pressure Res. **27**, 431 (2007).

[81] D. E. Grady, in *High-Pressure Research: Applications to Geophysics*, edited by M. H. Manghnani and S. Akimoto (Academic Press, San Diego, CA, 1977), pp. 389–438; J. Geophys. Res. **85**, 913 (1980).

[82] T. S. Duffy and T. J. Ahrens, J. Geophys. Res. **100**, 529 (1995).

[83] B. Li, K. Woody, and J. Kung, J. Geophys. Res. **111**, B11206 (2006).

[84] T. S. Sokolova, P. I. Dorogokupets, and K. D. Litasov, Russian Geol. Geophys. **54**, 181 (2013).

[85] K. D. Litasov *et al.*, J. Appl. Phys. **113**, 093507 (2013), Table IV.

[86] *Weighted Least Squares Regression*, Section 4.1.4.3 of *NIST/SEMATECH e-Handbook of Statistical Methods*, http://www.itl.nist.gov/div898/handbook/, December 3, 2017.

[87] J. R. Taylor, *An Introduction to Error Analysis*, 2nd ed. (University Science Books, Sausalito, CA, 1997), p. 166.

[88] O. V. Fat'yanov, T. Ogura, M. F. Nicol, and K. Kondo, AIP Conf. Proc. **505**, 959 (2000); O. V. Fat'yanov, T. Ogura, M. F. Nicol, K. G. Nakamura, and K. Kondo, Appl. Phys. Lett. **77**, 960 (2001).

[89] S. B. Kormer, M. V. Sinitsyn, and A. I. Kuryapin, Zh. Eksp. Teor. Fiz. **55**, 1626 (1968) [Sov. Phys. JETP **28**, 852 (1969)].

[90] V. D. Glukhodedov, S. I. Kirshanov, T. S. Lebedeva, and M. A. Mochalov, Zh. Eksp. Teor. Fiz. **116**, 551 (1999) [J. Exper. Theor. Phys. **89**, 292 (1999)].

[91] N. Yamada and S. Fujimura, in *Temperature, Its Measurement and Control in Science and Industry*, edited by J. F. Schooley (American Institute of Physics, New York, 1992), Vol. 6, pp. 843–847.

[92] P. P. Woskov and S. K. Sundaram, J. Appl. Phys. **92**, 6302 (2002).

[93] B. M. LaLone, G. D. Stevens, W. D. Turley, D. B. Holtkamp, A. J. Iverson, R. S. Hixson, and L. R. Veeser, J. Appl. Phys. **114**, 063506 (2013).

[94] P. M. Celliers, G. W. Collins, L. B. Da Silva, D. M. Gold, R. Cauble, R. J. Wallace, M. E. Foord, and B. A. Hammel, Phys. Rev. Lett. **84**, 5564 (2000).

[95] D. K. Bradley, J. H. Eggert, D. G. Hicks, P. M. Celliers, S. J. Moon, R. C. Cauble, and G. W. Collins, Phys. Rev. Lett. **93**, 195506 (2004).

[96] O. V. Fat'yanov and P. D. Asimow, *Equation of State and Observation of Partial Melting of B1 Phase MgO above 200 GPa from Shock Compression Experiments on Samples Preheated to 2300 K*, EOS Transactions AGU 97, Fall meeting supplement, abstract MR11A-2371 (2016), available at http://adsabs.harvard.edu/abs/2016AGUFMMR11A2371F.

[97] T. Qi, M. Millot, R. G. Kraus, S. Root, and S. Hamel, Phys. Plasmas **22**, 062706 (2015)

[98] S. N. Luo and T. J. Ahrens, Phys. Earth Planet. Inter. **143–144**, 369 (2004).

[99] J. H. Eggert, D. G. Hicks, P. M. Celliers, D. K. Bradley, R. S. McWilliams, R. Jeanloz, J. E. Miller, T. R. Boehly, and G. W. Collins, Nat. Phys. **6**, 40 (2010).

[100] S. B. Kormer, Usp. Fiz. Nauk **94**, 641 (1964) [Sov. Phys. Usp. **11**, 229 (1968)].

[101] S. B. Kormer, M. V. Sinitsyn, G. A. Kirillov, and V. D. Urlin, J. Exptl. Theoret. Phys. (USSR) **48**, 1033 (1965) [Sov. Phys. JETP **21**, 689 (1965)].

[102] M. Sanamzadeh, L. Tsang, J. T. Johnson, R. J. Burkholder, and S. Tan, J. Opt. Soc. Am. A **34**, 395 (2017).

[103] N. Fabricius, P. Hermes, D. von der Linde, A. Pospieszczyk, and B. Stritzker, Solid State Commun. **58**, 239 (1986).

[104] R. G. McQueen and J. N. Fritz, AIP Conf. Proc. **78**, 193 (1982).

[105] R. G. McQueen, in *Shock Compression of Condensed Matter 1991*, edited by S. C. Schmidt, R. D. Dick, J. W. Forbes, and D. G. Tasker (Elsevier, North Holland, 1992), p. 75.
[106] G. A. Lyzenga and T. J. Ahrens, Geophys. Res. Lett. **7**, 141 (1980).
[107] T. J. Ahrens, G. A. Lyzenga, and A. C. Mitchell, in *High-Pressure Research in Geophysics*, Advances in Earth and Planetary Sciences No. 12 (Kluwer, Boston, MA, 1982), pp. 579–594.
[108] G. A. Lyzenga, T. J. Ahrens, and A. C. Mitchell, J. Geophys. Res. **88**, 2431 (1983).
[109] D. G. Hicks, T. R. Boehly, J. H. Eggert, J. E. Miller, P. M. Celliers, and G. W. Collins, Phys. Rev. Lett. **97**, 025502 (2006).
[110] K. G. Holland and T. J. Ahrens, Science **275**, 1623 (1997).
[111] M. M. Budzevich, V. V. Zhakhovsky, C. T. White, and I. I. Oleynik, Phys. Rev. Lett. **109**, 125505 (2012); AIP Conf. Proc. **1426**, 1267 (2012).
[112] B. Rethfeld, K. Sokolowski-Tinten, D. von der Linde, and S. I. Anisimov, Phys. Rev. B **65**, 092103 (2002).
[113] K. Lu and Y. Li, Phys. Rev. Lett. **80**, 4474 (1998).
[114] M. M. Martynyuk, Thermochimica Acta **206**, 55 (1992).
[115] D. Ma and Y. Li, J. Phys.: Condens. Matter **12**, 9123 (2000).
[116] (a) Y. Shen, S. B. Jester, T. Qi, and E. J. Reed, Nat. Mater. **15**, 60 (2016); (b) Y. Shen and E. J. Reed, J. Phys. Chem. C **120**, 17759 (2016).
[117] R. G. McQueen, J. N. Fritz, and S. P. Marsh, J. Geophys. Res. **68**, 2319 (1963).
[118] A. E. Gleason, C. A. Bolme, H. J. Lee, B. Nagler, E. Galtier, D. Milathianaki, J. Hawreliak, R. G. Kraus, J. H. Eggert, D. E. Fratanduono, G. W. Collins, R. Sandberg, W. Yang, and W. L. Mao, Nat. Commun. **6**, 8191 (2015).
[119] A. B. Belonoshko, Geochim. Cosmochim. Acta **58**, 1557 (1994); A. B. Belonoshko and L. S. Dubrovinsky, *ibid.* **59**, 1883 (1995).
[120] Y. Usui and T. Tsuchiya, J. Earth Sci. **21**, 801 (2010).
[121] P. D. Asimow, M. C. Akin, M. Homel, R. S. Crum, D. Pagan, J. Lind, J. Bernier, J. L. Mosenfelder, A. M. Dillman, B. Lavina, S. Lee, O. V. Fat'yanov, and M. G. Newman, *Phase Transitions and Melting on the Hugoniot of* Mg_2SiO_4 *Forsterite: New Diffraction and Temperature Results*, American Physical Society Topical Group meeting on Shock Compression of Condensed Matter, St. Louis, MO (2017), abstract available at http://meetings.aps.org/Meeting/SHOCK17/Session/F5.3
[122] R. Boehler, M. Ross, and D. B. Boercker, Phys. Rev. Lett. **78**, 4589 (1997).
[123] M. G. Gorman, R. Briggs, E. E. McBride, A. Higginbotham, B. Arnold, J. H. Eggert, D. E. Fratanduono, E. Galtier, A. E. Lazicki, H. J. Lee, H. P. Liermann, B. Nagler, A. Rothkirch, R. F. Smith, D. C. Swift, G. W. Collins, J. S. Wark, and M. I. McMahon, Phys. Rev. Lett. **115**, 095701 (2015).
[124] C. A. Swenson, J. W. Shaner, and J. M. Brown, Phys. Rev. B **34**, 7924 (1986).
[125] R. Boehler, M. Ross, and D. B. Boercker, Phys. Rev. B **53**, 556 (1996).
[126] S. B. Kormer, K. B. Yushko, and G. V. Krishkevich, Pis'ma Zh. Eksp. Teor. Fiz. **3**, 64 (1966) [JETP Lett. (USSR) **3**, 39 (1966)].